

### 3D-Herschel: Constraining Dust Emission with Panchromatic Modeling of 3D-HST Galaxies

SEAMUS McNULTY,<sup>1</sup> MIMI SONG,<sup>1</sup> KATHERINE E. WHITAKER,<sup>1,2</sup> JOEL LEJA,<sup>3,4,5</sup> AUBREY MEDRANO,<sup>1</sup>  
ELIJAH P. MATHEWS,<sup>3,4,5</sup> MARK DICKINSON,<sup>6</sup> HANA E. INAMI,<sup>7</sup> IVO LABBE,<sup>8</sup> DANILO MARCHESINI,<sup>9</sup> ALEXANDRA POPE,<sup>1</sup> AND  
IRENE SHIVAEI<sup>10,11</sup>

<sup>1</sup>*Department of Astronomy, University of Massachusetts, Amherst, MA, 01003 USA*

<sup>2</sup>*Cosmic Dawn Center (DAWN), Niels Bohr Institute, University of Copenhagen, Jagtvej 128, København N, DK-2200, Denmark*

<sup>3</sup>*Department of Astronomy & Astrophysics, The Pennsylvania State University, University Park, PA 16802, USA*

<sup>4</sup>*Institute for Computational & Data Sciences, The Pennsylvania State University, University Park, PA 16802, USA*

<sup>5</sup>*Institute for Gravitation and the Cosmos, The Pennsylvania State University, University Park, PA 16802, USA*

<sup>6</sup>*NSF's National Optical-Infrared Astronomy Research Laboratory, 950 N. Cherry Avenue, Tucson, AZ 85719, USA*

<sup>7</sup>*Hiroshima Astrophysical Science Center, Hiroshima University, 1-3-1 Kagamiyama, Higashi-Hiroshima, Hiroshima 739-8526, Japan*

<sup>8</sup>*Centre for Astrophysics and Supercomputing, Swinburne University of Technology, Melbourne, VIC 3122, Australia*

<sup>9</sup>*Department of Physics and Astronomy, Tufts University, 574 Boston Ave., Medford, MA 02155, USA*

<sup>10</sup>*Centro de Astrobiología (CAB), CSIC-INTA, Carretera de Ajalvir km 4, Torrejón de Ardoz 28850, Madrid, Spain*

<sup>11</sup>*Steward Observatory, University of Arizona, Tucson, AZ 85721, USA*

#### Abstract

We present 3D-Herschel, a new 0.3-350 $\mu$ m photometric catalog that combines deblended Herschel far-infrared (FIR) imaging with the CANDELS/3D-HST legacy fields to probe the dust-obscured universe. Using the 17-parameter fitting code `PROSPECTOR- $\beta$` , a Bayesian inference framework, we model 41,387 galaxies spanning  $0.5 < z < 2.5$  to measure stellar and dust properties with realistic error bars. Comparing fits with and without FIR constraints, we find that for the 3.2% of galaxies with  $> 3\sigma$  detections in at least two Herschel bands, UV-MIR-only models (0.3-24 $\mu$ m) recover robust stellar ages, SFRs, and stellar masses (50-70% within the median  $1\sigma$  error). Consequently, the star-forming sequence shows no systematic offset, with an average deviation of  $0.1 \pm 0.07$  dex at fixed stellar mass for FIR-detected sources at all redshifts. However, the use of rigid log-average IR templates with fixed dust emission parameters ( $\gamma$ ,  $U_{\min}$ ,  $Q_{\text{PAH}}$ ) in UV-MIR modeling corresponds to an unevolving MIR-to-IR luminosity ratio and cold dust temperatures. By contrast, fits that include Herschel photometry, with added freedom in the FIR, yield dust temperatures that are  $\sim 7\text{K}$  warmer at all redshifts, with  $\sim 0.2$  dex higher IR-to-7.7 $\mu$ m luminosity ratios at the low-mass end of a Herschel-detected sample ( $\log(M_*) \sim 9.6 M_{\odot}$ ). These results demonstrate that MIR-to-IR conversions depend on stellar mass, cautioning against  $L_{\text{IR}}$ -independent templates without FIR data. For galaxies with  $< 10^{11} M_{\odot}$  at  $z > 1.5$ , even with state-of-the-art analysis, Herschel can at best provide upper limits due to source confusion; next-generation FIR telescopes will be essential to fully characterize dust emission in distant galaxies.

*Keywords:* galaxies: photometry, galaxies: fundamental parameters, infrared: galaxies, (ISM:) dust, extinction, galaxies: star formation

#### 1. INTRODUCTION

Studying galaxy properties during the epoch leading up to cosmic noon ( $z \sim 1 - 3$ ), which marks the peak of cosmic star formation (Madau & Dickinson 2014), pro-

vides crucial insights into the physical processes that drive their growth and evolution (e.g., Behroozi et al. 2013; van Dokkum et al. 2015). Because direct measurements of galaxy properties are not possible, astronomers rely on indirect methods, inferring stellar populations, dust, and gas from observed light. Much of this radiation is heavily attenuated by dust (Madau & Dickinson 2014; Casey et al. 2018), especially among the most

massive galaxies (Whitaker et al. 2017), with the complex interplay among different galaxy properties further complicating interpretation (e.g., Leja et al. 2019a). To disentangle these effects, models are fit to photometric data to reconstruct a galaxy’s spectral energy distribution (SED) (Johnson et al. 2021; Carnall et al. 2018; Iyer et al. 2019). Constraining these models requires broad photometric coverage, ideally spanning the rest-ultraviolet to far-infrared (UV–FIR), where both stellar and dust emission are captured (Conroy 2013).

Some of the deepest FIR windows into the universe (70–350 $\mu$ m) lie within the Cosmic Assembly Near-infrared Deep Extragalactic Legacy Survey (CANDELS)/3D-HST extragalactic fields (Grogin et al. 2011; Koekemoer et al. 2011; Skelton et al. 2014; Momcheva et al. 2016), regions that were already heavily targeted by Spitzer Space Telescope and Herschel Space Observatory to probe the dust-emission regime where most stellar light is reprocessed. While public FIR-selected catalogs exist for almost all Herschel surveys in these fields (e.g., Roseboom et al. 2010; Elbaz et al. 2011; Oliver et al. 2012; Magnelli et al. 2013; Jin et al. 2018; Liu et al. 2018), simple cross-matching with ultraviolet to near-infrared (NIR) catalogs will not yield robust photometry due to severe blending issues caused by the low-resolution nature of the data. Instead, “forced photometry”, which uses source positions and light profiles from a higher resolution prior, identifies roughly 50% more FIR-bright galaxies and enables an analysis reaching fainter fluxes than is otherwise possible (e.g., Lang et al. 2016).

Combining Herschel’s long wavelength coverage through forced photometry with the existing high-quality 3D-HST photometric catalogs (Skelton et al. 2014), yields a powerhouse dataset of broadband/medium-band space- and ground-based photometry supported by grism spectroscopy (Momcheva et al. 2016). A UV–FIR photometric catalog enables stellar population synthesis (SPS) modeling of galaxy SEDs observed during the most dust-obscured, star-forming epoch of the universe.

SPS techniques aimed at recovering integrated galaxy properties are extensive and rely on large encompassing stellar spectral libraries. Because galaxy parameters are interdependent, models must adopt diverse parameterizations and priors, increasing their dimensionality. Early SPS models were limited to four to six parameters, leaving significant systematic uncertainties (Brinchmann & Ellis 2000; Papovich et al. 2001; Shapley et al. 2001; Salim et al. 2007; Kriek et al. 2009; Maraston et al. 2010; Acquaviva et al. 2011). More recently, models have begun to capture the additional complexities

of galaxies, with high-dimensional ( $N \gtrsim 7$ ), computationally efficient frameworks only now becoming widely incorporated into SPS studies (Han & Han 2014; Leja et al. 2019a; Boquien, M. et al. 2019; Bowman et al. 2020).

Modern SPS models have evolved significantly, particularly with the integration of Bayesian inference methods, enabling more realistic measurements by leveraging priors to capture uncertainties and constraints. A recent versatile framework, *Prospector- $\beta$*  (Wang et al. 2023), is a 17-parameter physical model that includes a nonparametric star formation history (SFH), a two-component dust attenuation model, and dust emission powered via energy balance (Da Cunha et al. 2008). This flexibility addresses limitations of earlier models, which often relied on parametric SFHs and fixed dust attenuation curves, imposing strong priors that biased key galaxy properties. For instance, Carnall et al. (2019) show that different SFH models can shift inferred stellar masses, star formation rates (SFRs), and mass-weighted ages by  $\gtrsim 0.1$ , 0.3, and 0.2 dex, respectively, whereas these discrepancies are minimized when codes adopt flexible SFHs (e.g., Pacifici et al. 2023). Similarly, the adoption of a universal dust attenuation curve is known to result in underestimates of stellar masses (and overestimates of specific SFRs), particularly in dusty systems (Kriek & Conroy 2013).

In contrast, the nonparametric SFH adopted by *Prospector- $\beta$*  does not impose a fixed functional shape, making the recovered SFHs less prone to spurious, prior-driven fluctuations and more representative of the underlying data (Carnall et al. 2019). *Prospector- $\beta$* ’s two-component dust model accounts for both attenuation from dusty natal clouds around young stars and diffuse dust in the interstellar medium (ISM) that affects all stars (Leja et al. 2017; Conroy 2013), enabling it to capture a broader range of dust conditions when combined with the original dust attenuation model from Charlot & Fall (2000).

The framework also allows Polycyclic Hydrocarbon Aromatic (PAH) strengths to vary, rather than fixing them as common in lower-dimensional models (Leja et al. 2017, 2019b; Abdurro’uf et al. 2021), and this capability is now implemented in the full 17-parameter *Prospector- $\beta$*  framework (Wang et al. 2023). PAHs absorb UV and optical photons and reradiate them as strong mid-infrared (MIR) features, so varying PAH strengths in the model enable more realistic estimates of dust attenuation and re-emission (Draine & Li 2007). Together, the nonparametric SFH and flexible dust treatment help mitigate degeneracies among dust, age,

and mass, reducing the systematic biases that limited earlier models (Leja et al. 2019a; Carnall et al. 2019).

Due to the nonparametric SFH, two-component dust model, and flexible attenuation curve, `Prospector` yields more self-consistent SFR estimates (Leja et al. 2022), in contrast to those inferred by combined rest-UV and IR fluxes (Daddi et al. 2007; Kennicutt & Evans 2012; Whitaker et al. 2012, 2014). While UV+IR estimates remain broadly consistent for actively star-forming systems, they can overestimate SFRs in suppressed systems by up to  $\sim 1$  dex (Utomo et al. 2014; Hayward & Smith 2015; Fumagalli et al. 2014). At  $\log(M_\star/M_\odot) > 9.5$ , dust emission dominates the radiative output of active star-forming galaxies (Whitaker et al. 2017), but in more passive systems, `Prospector` disentangles dust heating from older ( $t > 100$  Myr) stars, yielding SFRs lower by  $\sim 0.1$ – $1$  dex (Leja et al. 2019b). By modeling these subtleties, `Prospector` therefore re-attributes some of the observed IR light to dust heating from older stars, breaking degeneracies among dust, age, and stellar mass. As a result, Leja et al. (2022) find the star-forming main sequence (SFMS) inferred by this framework lies  $\sim 0.2$ – $0.5$  dex below traditional UV+IR estimates, implying an older and more massive universe.

However, recent studies using modern methods remain limited to UV-MIR coverage (Leja et al. 2019b, 2022; Mathews et al. 2023; Shivaie et al. 2024), with the reddest filters reaching only  $24\mu\text{m}$  and lacking constraints on the IR SED past this. Yet redward of rest-frame  $50\mu\text{m}$ , dust emission makes up about two-thirds of the total IR luminosity (Conroy 2013). To compensate, Leja et al. (2022) adopt a fixed IR template in their `Prospector` models, using its shape to derive the total IR luminosity and thereby the SFR (Leja et al. 2019a). Without direct FIR constraints, degeneracies among age, dust, and metallicity remain difficult to resolve, as all reddened galaxy colors (Papovich et al. 2001).

At the time of Herschel’s launch, the possibility of directly constraining  $L_{\text{IR}}$ , and thus incorporating FIR emission into full SED modeling, represented a major advance in quantifying dust emission (e.g., Burgarella et al. 2005; Noll, S. et al. 2009) and breaking long-standing degeneracies. Early Herschel results showed tight correlations between MIR and total IR luminosity (e.g., via the IR8 relation; Elbaz et al. 2011; Reddy et al. 2011), which motivated the construction of fixed IR templates (e.g., Whitaker et al. 2014). Subsequent work demonstrated that these templates must vary with physical conditions such as the PAH mass fraction, stellar mass, and redshift (Shivaie et al. 2017; Whitaker et al. 2017), pointing away from universal templates. Ultimately, however, Herschel’s PACS/SPIRE data are

strongly confusion-limited in deep extragalactic fields, preventing robust flux measurements for most individual galaxies and forcing reliance on templates or stacking. Overcoming this limitation requires improved positional and photometric priors to extract reliable fluxes below the confusion limit—an approach we adopt here by deblending the Herschel images to recover significantly higher FIR photometry.

In this paper, we present a comprehensive, long-wavelength analysis of how FIR data influence galaxy scaling relations using `Prospector` modeling. We deblend low-resolution Herschel images to incorporate FIR photometry into the 3D-HST photometric catalogs (Skelton et al. 2014; Momcheva et al. 2016), producing a new UV-FIR ( $0.3$ – $350\mu\text{m}$ ) dataset, 3D-Herschel. By jointly modeling UV-NIR starlight and dust re-emission in the MIR-FIR, we quantify the impact of adding FIR constraints to SPS modeling. Coupled with `Prospector`’s 17-parameter Bayesian framework, this approach improves constraints on dust emission and helps to mitigate well-known degeneracies in SPS modeling.

The paper is organized as follows. In §2, we describe the data used in this study, including the 3D-HST catalogs, Herschel observations, and the forced photometry methods employed to extract deblended FIR fluxes. §3 presents the validation of the new 3D-Herschel catalog. In §4 we present a comparison between `Prospector` fits for 3D-HST, and a more efficient emulator, adopted for the 3D-Herschel analysis. Results from the SED modeling are given in §5, with a higher-quality, IR-bright subsample analyzed in §6. We discuss the results in §7, with the conclusion presented in §8.

Throughout the paper, we adopt a concordance  $\Lambda\text{CDM}$  cosmology with  $H_0 = 70 \text{ km s}^{-1} \text{ Mpc}^{-1}$ ,  $\Omega_M = 0.3$ , and  $\Omega_\Lambda = 0.7$ . We use a Chabrier (2003) initial mass function (IMF) between  $0.1 M_\odot$  and  $100 M_\odot$ . We refer to the Hubble Space Telescope (HST) bands F435W, F606W, F775W, F814W, F850LP, F098M, F105W, F125W, F140W, and F160W as  $B_{435}$ ,  $V_{606}$ ,  $i_{775}$ ,  $I_{814}$ ,  $z_{850}$ ,  $Y_{098}$ ,  $Y_{105}$ ,  $J_{125}$ ,  $JH_{140}$ , and  $H_{160}$ , respectively. All uncertainties are quoted at the 68% confidence level.

## 2. DATA

### 2.1. 3D-HST/CANDELS

The parent sample for this study originates from the public multi-wavelength 3D-HST photometric catalog,

**Table 1.** Summary of Herschel programs

Field	Area (arcmin <sup>2</sup> ) <sup>e</sup>	Survey		70 $\mu$ m	100 $\mu$ m	160 $\mu$ m	250 $\mu$ m	350 $\mu$ m
		PACS	SPIRE					
GOODS-S	177	GOODS-H, PEP	HerMES	0.3 <sup>a</sup>	0.2 <sup>a</sup>	0.4 <sup>a</sup>	0.9 <sup>d</sup>	0.8 <sup>d</sup>
GOODS-N	164	GOODS-H, PEP	GOODS-H	–	0.3 <sup>a</sup>	0.7 <sup>a</sup>	1.9 <sup>c</sup>	2.4 <sup>c</sup>
COSMOS	199	CANDELS-H, PEP	CANDELS-H	–	0.5 <sup>b</sup>	1.0 <sup>b</sup>	1.6 <sup>f</sup>	1.3 <sup>f</sup>
UDS	201	CANDELS-H	CANDELS-H	–	2.2 <sup>g</sup>	3.4 <sup>b</sup>	2.2 <sup>f</sup>	1.9 <sup>f</sup>

<sup>a</sup>Depths for GOODS-S and GOODS-N bands are taken from the PEP public data release documentation.

<sup>b</sup>Depths for UDS and COSMOS PACS bands are taken from Popesso et al. (2019).

<sup>c</sup>From Elbaz et al. (2011).

<sup>d</sup>From Oliver et al. (2012).

<sup>e</sup>From Skelton et al. (2014).

<sup>f</sup>From <http://www.astrodeep.eu/data/>.

<sup>g</sup>Estimated based on our flux comparisons (Figure 1), as the original source is direct detection from Spitzer, opposed to the forced photometry methods used in this study.

NOTE—Quoted depths are median  $1\sigma$  flux uncertainties for each field. For GOODS-S and GOODS-N, we list the depth in the deepest region.

covering 0.3–8 $\mu$ m (Skelton et al. 2014)<sup>1</sup>. The 3D-HST survey leverages imaging from the CANDELS program, designed to study galaxy evolution (Skelton et al. 2014; Momcheva et al. 2016). The original sample consists of  $\sim$ 166k sources detected in HST  $J_{125} + JH_{140} + H_{160}$  images covering  $\sim$ 740 arcmin<sup>2</sup> over the four deep CANDELS fields, COSMOS, GOODS-S, GOODS-N, UDS. Beyond this HST imaging, observations additionally include a suite of ground-based imaging, Spitzer 4–8 $\mu$ m IRAC forced photometry (Skelton et al. 2014), with a supplement of 24 $\mu$ m Spitzer/MIPS forced photometry supplied by Whitaker et al. (2014). There are up to 45 total photometric bands in the original catalogs.

The Spitzer/MIPS 24 $\mu$ m photometry presented by Whitaker et al. (2014) was derived using a forced-photometry approach closely analogous to that adopted for the Herschel imaging in this work. High resolution HST/WFC3 imaging was used as a positional and morphological prior, enabling fluxes to be measured at fixed source positions while modeling and deblending contributions from neighboring objects in the low-resolution MIPS data. The HST detection images were PSF-matched to the F160W resolution and rebinned to account for the large MIPS point-spread function (FWHM  $\approx$  6", comparable to that of Herschel/PACS at 100 $\mu$ m). Photometry was performed using the Multi-resolution Object PHotometry oN Galaxy Observa-

tions (MOPHONGO; Labbé et al. 2006) code, which simultaneously fits all sources within each beam using position-dependent convolution kernels, thereby mitigating source confusion and blending. This methodology is directly relevant to the challenges inherent to Herschel photometry, where similarly large beam sizes necessitate the use of high-resolution priors for robust flux extraction.

Slitless spectroscopy covers  $\sim$ 75% of the CANDELS area, providing redshift estimates with precisions of order  $\frac{\Delta z}{1+z} \sim 0.003$  when combined with broad and medium-band photometry (Skelton et al. 2014; Momcheva et al. 2016). We adopt redshifts,  $z_{\text{best}}$ , from Momcheva et al. (2016), which are ranked in order depending on their availability. The 'best' starting with ground-based spectroscopic redshifts, next space-based grism redshifts provided by the 3D-HST grism survey (Momcheva et al. 2016), and finally otherwise photometric redshifts estimated from the EAZY photometric redshift code (Brammer et al. 2008). We refer the reader to Skelton et al. (2014) and Momcheva et al. (2016) for a full description of the 3D-HST data and catalog construction.

## 2.2. Herschel data

We use the deepest available Herschel imaging obtained with PACS (70–160 $\mu$ m) and SPIRE (250–350 $\mu$ m) in four CANDELS fields. The key Herschel programs used in this study are the Great Observatories Origins Deep Survey-Herschel (GOODS-Herschel) (PI D. Elbaz;

<sup>1</sup> <http://3dhst.research.yale.edu>

Elbaz et al. 2011) and CANDELS-Herschel (PI M. Dickinson). These two surveys are the deepest Herschel observations to extend the capabilities of CANDELS/3D-HST by incorporating FIR observations, aiming to probe typical star-forming galaxies up to  $z \sim 2$ .

In brief, the GOODS-Herschel survey obtained both PACS and SPIRE imaging in the GOODS-N region, contributing to a comprehensive dataset for this field. In GOODS-S, the survey focused on obtaining ultradeep PACS imaging in a sub-region of  $10' \times 10'$ . Likewise, the CANDELS-Herschel covers the COSMOS and UDS fields, both in PACS and SPIRE, to a comparable depth to the GOODS fields.

We also utilize Herschel data from the PACS Evolutionary Probe (PEP) and the Herschel Multi-tiered Extragalactic Survey (HerMES). PEP is a survey conducted with PACS, spanning over  $2.7 \text{ deg}^2$  targeting well-known extragalactic fields, including the CANDELS fields (Lutz et al. 2011), while HerMES covers a wide area of  $70 \text{ deg}^2$ , with both the PACS and SPIRE instruments (Oliver et al. 2012).

The Herschel PACS and SPIRE maps used in this work for GOODS-N, COSMOS, and UDS, as well as PACS-only maps for GOODS-S, were constructed by H. Inami (private communication) by combining observations from the GOODS-H, CANDELS-H, and PEP surveys. For GOODS-S SPIRE data, we instead use the public HerMES maps. Table 1 lists the area, programs, and  $1\sigma$  depths for the Herschel images used in this study.

We do not include the AEGIS field in the present analysis because the corresponding photometric catalog could not be independently validated to the same standard as the other 3D-HST fields. Comparisons with external Herschel-based catalogs show large systematic discrepancies in the SPIRE fluxes ( $\sim 2$  magnitudes), indicating unresolved calibration or reduction issues. Resolving these discrepancies would require a full reprocessing of the AEGIS Herschel data, which is beyond the scope of this paper.

### 2.2.1. Forced photometry

Due to the shallow depth and large point spread function (PSF) of Herschel imaging (PSF FWHM  $\sim 7\text{-}25''$ ), confusion noise dominates the images. The cosmic FIR background, generated by faint unresolved sources, sets a limit below which individual sources cannot be detected. As a result, bright nearby objects blend together while faint ones are buried in the confusion noise, leaving FIR photometry of distant galaxies limited and noise-dominated (Pope et al. 2008).

Because of this severe blending, it is challenging to identify and stack clean point sources directly from the

science field. As a result, a high signal-to-noise empirical PSF cannot be constructed (as is possible for Spitzer data in, e.g., Whitaker et al. 2014). Instead, we adopt the calibration PSF of the asteroid Vesta<sup>2</sup>, which provides an uncontaminated and high S/N model of Herschel’s PSF shape. This ensures that the PSF model used in fitting and subtraction is accurate, thus improving deblending and flux recovery despite the large beam. For the field/bands where the Herschel data are heterogeneous and combine multiple scan directions and depths (i.e., GOODS-S PACS) the effective PSF varies across the mosaic. In these cases, we generate position-dependent PSFs that account for the position angles and the integration time of the telescope visit over the fields. This improves the clean subtraction of nearby sources, thereby achieving more accurate flux estimates for faint sources that fall in the PSF wings of brighter sources. These Herschel PSFs are then fed into MOPHONGO to construct transfer kernels between the HST detection and Herschel images.

To further mitigate source blending, we perform forced photometry on the mosaics in the four CANDELS fields. Contamination from neighboring objects is modeled using HST NIR imaging as positional priors and FIR flux predictions from Prospector FUV-MIR SED modeling (Leja et al. 2017) as flux priors. Incorporating these priors identifies more FIR-bright galaxies (Lang et al. 2016) and thus removes their contamination with higher fidelity, thereby boosting signal-to-noise and improving flux measurements for faint sources that lie below the confusion limit.

In the Herschel photometric extraction, we use T-PHOT (Merlin et al. 2015, 2016), incorporating FIR Prospector predictions and their uncertainties as Gaussian priors. Following the fitting approach described in Section 2.4 of Merlin et al. (2016), these priors are incorporated into the T-PHOT fitting as a regularization term on the source fluxes, while the Herschel fluxes themselves remain free parameters. The prior information helps stabilize the solution in confusion-limited regimes by suppressing degenerate flux assignments among deblended sources when the Herschel data alone are insufficient, while allowing the data to dominate the fit for well-detected objects.

FIR predictions from Prospector FUV-MIR modeling are available for galaxies at  $0.5 < z < 2.5$  above the 3D-HST mass completeness limit of  $\log(M_*/M_\odot) = 9.3$  (Tal et al. 2014), which comprises  $>93\%$  of FIR de-

<sup>2</sup> <https://www.cosmos.esa.int/web/herschel/ancillary-data-products>

tected sources (at least two Herschel filters detected) and 33% of sources in our entire sample (Leja et al. 2019b). For galaxies without individual `Prospector` predictions, we adopt priors based on the median predictions of sources at similar redshift ( $z_{\text{best}}$ ) and MIPS  $24\mu\text{m}$  flux.

For sources outside the  $0.5 < z < 2.5$  window studied in Leja et al. (2019b), we assign priors by extrapolating the median `Prospector` observed-frame  $24\mu\text{m}$ -to-Herschel flux ratios within that range. This approach, which Leja et al. (2019b) adopt with `Prospector- $\alpha$`  modeling, fixes the parameters in the IR SED from Draine & Li (2007) to exactly match the inferred conversion factors ( $L_8/L_{\text{IR}}$ ) from early Herschel studies (e.g., Elbaz et al. 2011) in an attempt to have no redshift evolution.

With the imposed position and flux priors described above, we model the Herschel imaging for our sample in the 3D-HST catalog with `T-PHOT`. We use Herschel images that are registered to the reference HST image and rebinned to the same pixel scale ( $0''.18/\text{pixel}$  and  $0''.36/\text{pixel}$  for PACS and SPIRE images, respectively) as input. In `T-PHOT`, the HST segmentation map is convolved with a transfer kernel to construct models for the low-resolution data (i.e., Herschel) for each source, with the flux of each source being left free to vary. The best-fit Herschel fluxes are then obtained by fitting these models to the observed Herschel data. While `T-PHOT` provides best-fit flux estimates for all sources, in this work we use the resulting source models to subtract contaminating neighbors.

### 2.2.2. Aperture photometry

Using the cleaned images produced by subtracting the best-fit `T-PHOT` models of neighboring sources, we measure final Herschel fluxes via aperture photometry. In brief, we construct a tile of a size of  $\sim 9$  times the PSF full-width half maximum (FWHM) for PACS100 and  $\sim 7$  times the FWHM for SPIRE350 centered on each source. We then perform aperture photometry of the central source in a radius of  $\sim 0.5$  PSF FWHM (e.g.,  $3''$  in PACS70,  $12''$  in SPIRE350) in the cleaned `T-PHOT` image. The measured flux is corrected for the finite size of the PSF, determined by comparing the curve-of-growth of the reference PSF of the asteroid Vesta. For the PSF size adopted in this study, this correction is  $\lesssim 10\%$ <sup>3</sup>. An additional correction is then applied to ac-

<sup>3</sup> 12,14,15,6,4% for PACS70, PACS100, PACS160, SPIRE250, SPIRE350, respectively

**Table 2.** Best-fit  $r\text{-}\sigma_f$  relation

Band	a	b
SPIRE250	-0.56	2.11
SPIRE350	-0.64	2.62

NOTE— The best-fit for the correction factor ( $r$ ) as a function of flux uncertainties ( $\sigma_f$ ) obtained in our Monte Carlo simulations, modeled as  $\log r = a \times \log \sigma_f + b$ , which is applied to the original flux errors in SPIRE bands.

count for flux loss of 11–13% due to high-pass filtering in PACS bands following Popesso et al. (2012)<sup>4</sup>.

### 2.2.3. Error budget

One source of uncertainty that may not be properly accounted for in our adopted scheme of post-`T-PHOT` aperture photometry is the uncertainties of flux priors. The flux prior uncertainty will become increasingly important at the longest wavelengths where resolution is poorest and blending is most severe.

Although the neighbor-subtracted residual image is derived from the single best-fit `T-PHOT` solution, this residual does not automatically propagate the uncertainty in the flux priors of neighboring sources into the cleaned image. To assess the impact of neighbor flux uncertainty on our aperture photometry—and to evaluate whether our measured flux uncertainties are realistic—we run Monte Carlo simulations in which we randomly perturb the fluxes of nearby sources following the Gaussian probability distribution of their flux priors as described in Section 2.2.1. We then build the corresponding residual map where the nearby sources are subtracted and the flux density of the central source is measured. We repeat the procedure 30 times for each of the  $\gtrsim 100$  sources for each field/band, which are selected to be uniformly distributed in SNR ( $0 < \text{SNR} < 20$  in PACS100).

The standard deviation of the output flux distribution obtained from the above procedure relative to the orig-

<sup>4</sup> 13,12,11% for PACS70, PACS100, PACS160, respectively

**Table 3.** Image sources

Field	Filters	Telescope/Instrument	Survey	Reference	
COSMOS	$u, g, r, i, z$	CFHT/MegaCam	CFHTLS	Erben et al. (2009); Hildebrandt et al. (2009)	
	$B, V, r', i', z'$ , 12 medium-band optical	Subaru/Suprime-Cam		Taniguchi et al. (2007)	
	F606W, F814W	HST/ACS	CANDELS	Grogin et al. (2011); Koekemoer et al. (2011)	
	$J1, J2, J3, H1, H2, K$	KPNO 4m/NEWFIRM	NMBS	Whitaker et al. (2011)	
	$J, H, K_s$	CFHT/WIRCam	WIRDS	Bielby et al. (2012)	
	$Y, J, H, K_s$	VISTA	UltraVISTA	McCracken et al. (2012)	
	F140W	HST/WFC3	3D-HST	Brammer et al. (2012)	
	F125W, F160W	HST/WFC3	CANDELS	Grogin et al. (2011); Koekemoer et al. (2011)	
	3.6, 4.5 $\mu$ m	Spitzer/IRAC	SEDS	Ashby et al. (2013)	
	5.8, 8 $\mu$ m	Spitzer/IRAC	S-COSMOS	Sanders et al. (2007)	
	24 $\mu$ m	Spitzer/MIPS	S-COSMOS	Sanders et al. (2007)	
	100, 160 $\mu$ m	Herschel/PACS	CANDELS-H, PEP	H. Inami (Priv. Comm)	
	250, 350 $\mu$ m	Herschel/SPIRE	CANDELS-H	H. Inami (Priv. Comm)	
	GOODS-N	$U$	KPNO 4m/Mosaic	Hawaii HDFN	Capak et al. (2004)
$G, R_s$		Keck/LRIS		Steidel et al. (2003)	
F435W, F606W, F775W, F850LP		HST/ACS	GOODS	Giavalisco et al. (2004)	
$B, V, R_c, I_c, z'$		Subaru/Suprime-Cam	Hawaii HDFN	Capak et al. (2004)	
F140W		HST/WFC3	3D-HST	Brammer et al. (2012)	
F125W, F160W		HST/WFC3	CANDELS	Grogin et al. (2011); Koekemoer et al. (2011)	
$J, H, K_s$		Subaru/MOIRCS	MODS	Kajisawa et al. (2011)	
3.6, 4.5 $\mu$ m		Spitzer/IRAC	SEDS	Ashby et al. (2013)	
5.8, 8 $\mu$ m		Spitzer/IRAC	GOODS	Dickinson et al. (2003)	
24 $\mu$ m		Spitzer/MIPS	GOODS	Dickinson et al. (2003)	
100, 160 $\mu$ m		Herschel/PACS	GOODS-H, PEP	Magnelli et al. (2013), H. Inami (Priv. Comm)	
250, 350 $\mu$ m		Herschel/SPIRE	GOODS-H	Elbaz et al. (2011), H. Inami (Priv. Comm)	
GOODS-S		$U, R$	VLT/VIMOS	ESO/GOODS	Nonino et al. (2009)
		$U38, B, V, R_c, I$	WFI 2.2m	GaBoDs	Hildebrandt et al. (2006); Erben et al. (2005)
	14 medium bands	Subaru/Suprime-Cam	MUSYC	Cardamone et al. (2010)	
	F435W, F606W, F775W, F850LP	HST/ACS	GOODS	Giavalisco et al. (2004)	
	F606W, F814W, F850LP	HST/ACS	CANDELS	Grogin et al. (2011); Koekemoer et al. (2011)	
	F140W	HST/WFC3	3D-HST	Brammer et al. (2012)	
	F125W, F160W	HST/WFC3	CANDELS	Grogin et al. (2011); Koekemoer et al. (2011)	
	$J, H, K_s$	VLT/ISAAC	ESO/GOODS, FIREWORKS	Retzlaff et al. (2010), Wuyts et al. (2008)	
	$J, K_s$	CFHT/WIRCam	TENIS	Hsieh et al. (2012)	
	3.6, 4.5 $\mu$ m	Spitzer/IRAC	SEDS	Ashby et al. (2013)	
	5.8, 8 $\mu$ m	Spitzer/IRAC	GOODS	Dickinson et al. (2003)	
	24 $\mu$ m	Spitzer/MIPS	GOODS	Dickinson et al. (2003)	
	70, 100, 160 $\mu$ m	Herschel/PACS	GOODS-H, PEP	Magnelli et al. (2013), H. Inami (Priv. Comm)	
	250, 350 $\mu$ m	Herschel/SPIRE	HerMES	Oliver et al. (2012)	
	UDS	$U$	CFHT/MegaCam		Almaini/Foucaud in prep.
		$B, V, R_c, i', z'$	Subaru/Suprime-Cam	SXDS	Furusawa et al. (2008)
F606W, F814W		HST/ACS	CANDELS	Grogin et al. (2011); Koekemoer et al. (2011)	
F140W		HST/WFC3	3D-HST	Brammer et al. (2012)	
F125W, F160W		HST/WFC3	CANDELS	Grogin et al. (2011); Koekemoer et al. (2011)	
$J, H, K_s$		UKIRT/WFCAM	UKIDSS DR8	Almaini in prep.	
3.6, 4.5 $\mu$ m		Spitzer/IRAC	SEDS	Ashby et al. (2013)	
5.8, 8 $\mu$ m		Spitzer/IRAC	SpUDS	Dunlop in prep.	
24 $\mu$ m		Spitzer/MIPS	SpUDS	Dunlop in prep.	
100, 160 $\mu$ m		Herschel/PACS	CANDELS-H	H. Inami (Priv. Comm)	
250, 350 $\mu$ m		Herschel/SPIRE	CANDELS-H	H. Inami (Priv. Comm)	

NOTE—UV–8 $\mu$ m list is taken from Skelton et al. (2014)

inal flux errors indicates that our SPIRE uncertainties are underestimated, and thus corrected as follows.

We find a clear anti-correlation of this ratio ( $r$ ) with the original SPIRE band flux uncertainties ( $\sigma_f$ ), whereas no significant trend is found with flux or SNR. The best-fit for the ratio  $r$  as a function of flux uncertainty, modeled as  $\log r = a \times \log \sigma_f + b$ , is adopted as the scale factor needed to be applied to the original flux errors in SPIRE. Table 2 lists the best-fit parameters. The correction factor increases with wavelength, from  $r \sim 3$  in SPIRE250 to  $r \sim 6$  in SPIRE350 at  $\sigma_f = 1$  mJy, but no significant variations are seen between the four fields.

We perform a second test of the updated flux uncertainties in all PACS and SPIRE bands. We first check the residual maps to confirm that the background peaks at zero, and then compare the width of the residual flux distribution to our inferred errors. Whereas the SPIRE filters are fine, the residual widths in the PACS filters are consistently a factor of two larger than the reported noise. This indicates that the PACS flux uncertainties remain underestimated. We thus scale the PACS error using the width of the residual map divided by the original flux uncertainties as the factor. Together, these corrections are comparable to the factor of  $\sim 5$  derived from simulation-based uncertainty calibrations in the COSMOS catalog by Jin et al. (2018), with our analysis providing a complementary empirical basis for such an adjustment.

These corrections ensure conservative flux uncertainties that are inflated appropriately considering the low-resolution Herschel images. We caution that catastrophic failures in the flux priors may occur in individual cases. However, because the T-PHOT solution is ultimately constrained by the pixel-level noise properties of the low-resolution image, sources with intrinsic  $S/N < 1$  are driven toward fluxes consistent with the image noise rather than the prior model values. As such, the methodology is relatively insensitive to prior mismatches at flux levels below the detection threshold. The extracted Herschel FIR photometry is then combined with the 3D-HST photometric catalogs (Skelton et al. 2014) and the  $24\mu\text{m}$  Spitzer fluxes from Whitaker et al. (2014), forming a long-wavelength ( $0.3 - 350\mu\text{m}$ ) master catalog, 3D-Herschel. Table 3 lists the photometric bands, telescope/instruments, and surveys covering the four fields in 3D-Herschel, with references available for further details.

To verify that the Herschel photometry was correctly extracted, we cross-examine the sources in each field of the 3D-Herschel catalog with existing catalogs that contain an independent measure of the Herschel photometry. Table 4 presents the published catalogs used for validation of the 3D-Herschel photometry, as well as the number of objects in each field.

It is important to note that these comparison catalogs are constructed from different combinations of Herschel imaging data and therefore probe somewhat different depths and coverages than the maps used in this work. For example, the PACS catalogs of Magnelli et al. (2013) for the GOODS fields are derived from combined PACS observations from both the PEP and the GOODS-Herschel key programs and reach  $3\sigma$  depths as low as  $\sim 0.6\text{-}1.3$  mJy at  $100$  and  $160\mu\text{m}$  in the deepest regions, representing some of the deepest PACS blank field data available in these fields. In contrast, the SPIRE catalogs used in validation for GOODS-South (e.g., Roseboom et al. 2010) are based on early SPIRE imaging from the HerMES science demonstration phase, which covers wider areas but is confusion limited with typical  $3\sigma$  thresholds of  $\approx 17\text{-}20$  mJy at  $250\text{-}500\mu\text{m}$  based on HerMES measured confusion noise; Nguyen et al. (2010)). Consequently, while useful for validating bright SPIRE sources, this comparison catalog does not reach the same depth as our tailored GOODS-Herschel/CANDELS-Herschel SPIRE photometry.

The super-deblended catalogs of Liu et al. (2018) in GOODS-North and Jin et al. (2018) in COSMOS are based on prior-driven source extraction applied to deep Herschel imaging that substantially overlaps with the datasets analyzed here: in GOODS-North, both PACS and SPIRE photometry are derived from GOODS-Herschel (with PACS supplemented by PEP), while in COSMOS the PACS imaging similarly combines CANDELS-Herschel and PEP data and the SPIRE measurements are drawn from HerMES. Despite modest differences in SPIRE data, these catalogs employ comparable underlying Herschel imaging and prior-based deblending techniques, making them well suited for validating our measurements. For the UDS field, the comparison PACS and SPIRE photometry is taken from publicly released HerMES catalog products<sup>5</sup>, which are based on prior-extracted fluxes from HerMES PACS and SPIRE imaging (Oliver et al. 2012). These catalogs provide an external consistency check for our measurements.

<sup>5</sup> UDS\_PACSxID24.v1 and L4-UDS\_xID250\_DR2

### 3. VALIDATION

**Table 4.** 3D-Herschel Comparison Samples to Validate the Photometry

	GOODS-S	GOODS-N	COSMOS	UDS
Total Number of Objects	50,507	38,279	33,879	44,102
PACS Comparison Catalog	Magnelli et al. (2013)	GOODS-N “Super-deblended” catalog	COSMOS “Super-deblended” catalog	Oliver et al. (2012)
SPIRE Comparison Catalog	Roseboom et al. (2010)	(Liu et al. 2018)	(Jin et al. 2018)	Oliver et al. (2012)

NOTE—For GOODS-North and COSMOS, the same super-deblended catalogs were used for both PACS and SPIRE comparisons.

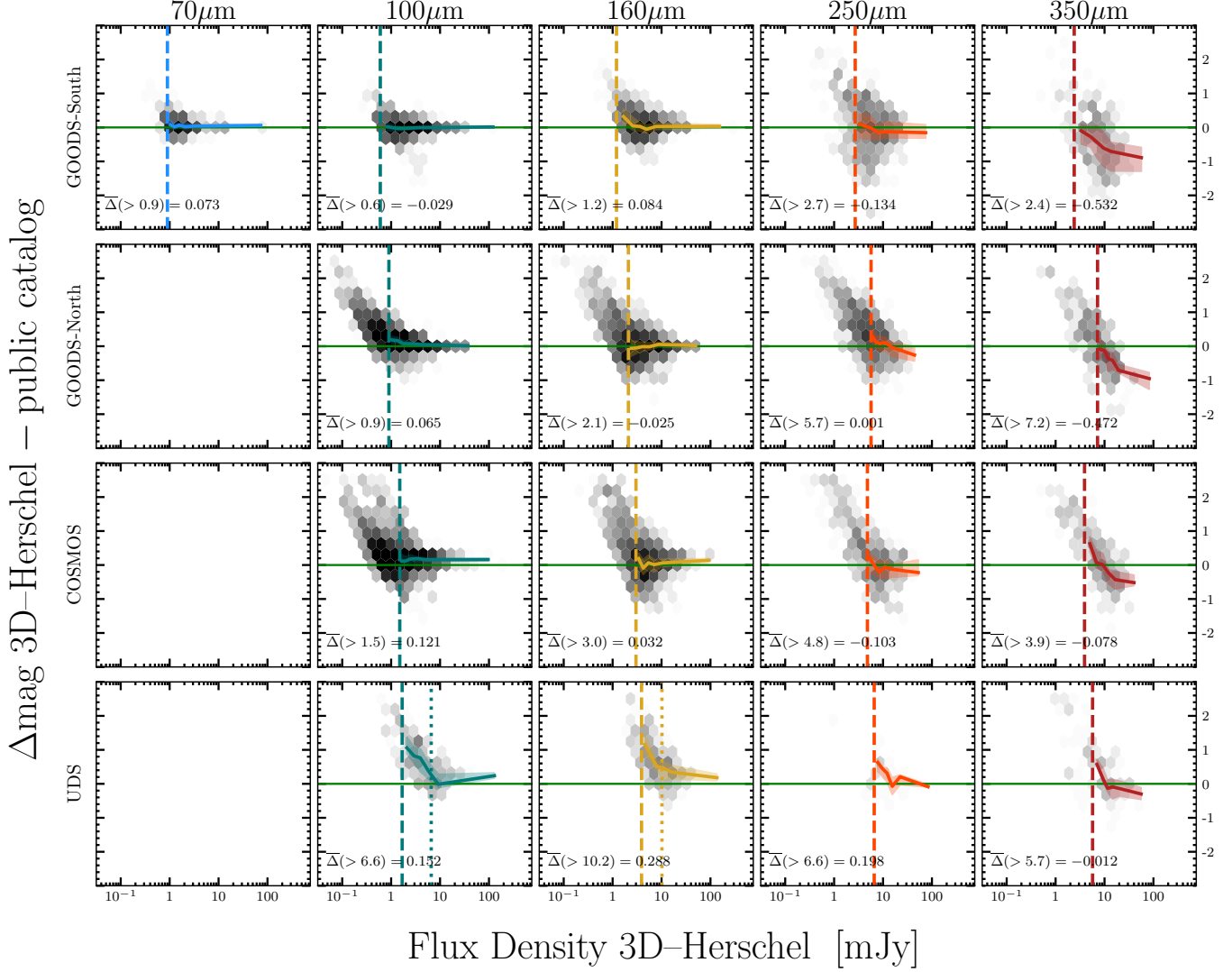


**Figure 1.** Overall agreement of 3D-Herschel fluxes compared to other published Herschel catalogs contained in the literature. The background color scale shows the logarithmic number density of sources in our sample. The dashed line indicates the median  $3\sigma$  flux uncertainty from the original survey publications, whereas the dotted lines are the limits we infer herein for sources originally detected with Spitzer, as opposed to the forced photometry methods assumed in this study (Table 1). The mean offset for objects above the  $3\sigma$  flux uncertainty is listed in the bottom left of each panel.

We compare fluxes between the deblended 3D-Herschel catalog and published catalogs by matching sources to the nearest object within a set radius in Fig-

ure 1. We apply  $\text{SNR} > 1$  to remove objects below the noise limit. For COSMOS, GOODS-N, and GOODS-S, we adopt a 0.5 arcsecond radius since the parent cat-

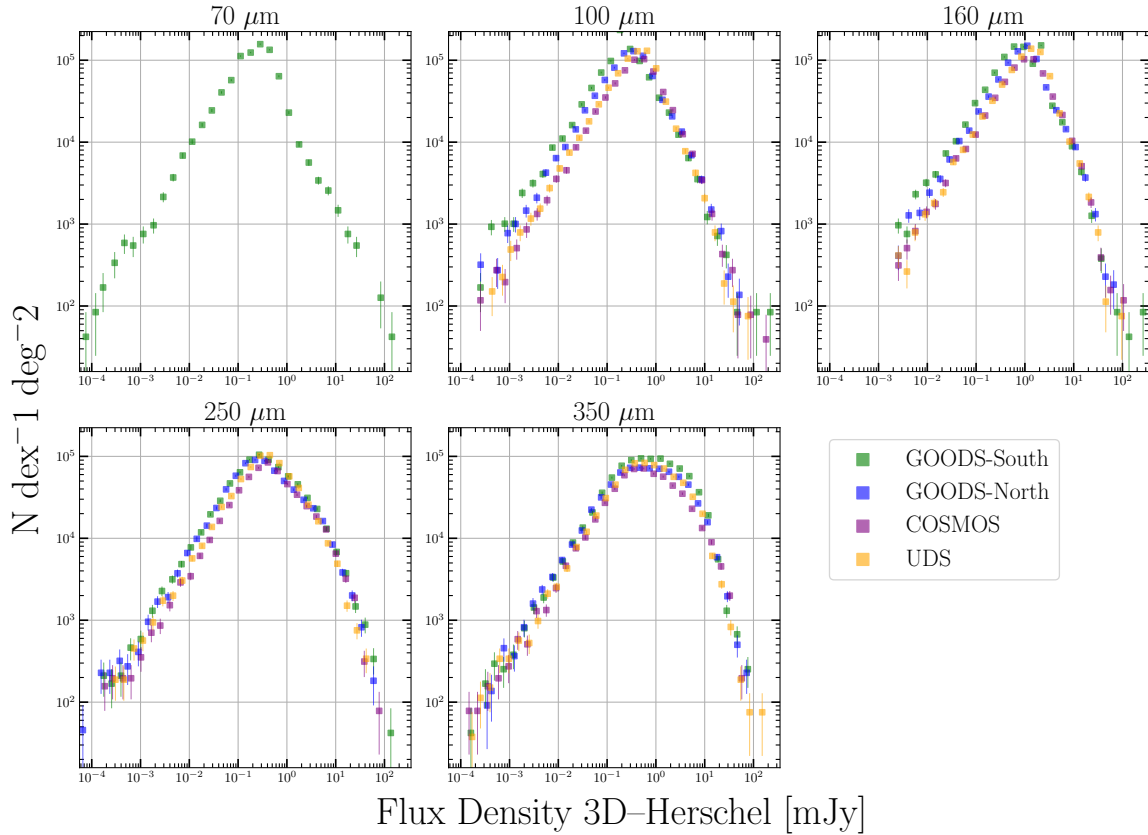


**Figure 2.** Close relationship between the number counts of each 3D-Herschel field (binned by flux) demonstrates that the photometric estimations were consistent across all fields. Error bars are determined as the fraction error of each bin ( $1/\sqrt{N} \times N \text{ dex}^{-1} \text{ deg}^{-2}$ ).

alogs are based on high-resolution imaging. For UDS, however, we use a 3 arcsecond radius, as sources are detected only at FIR wavelengths where positional uncertainties are comparable to the large pixel size. This larger matching radius compensates for potential positional offsets in the UDS field.

In general, we find that the 3D-Herschel catalog is in good agreement with other officially released catalogs, indicating the deblending process was successful and the fluxes are robustly extracted. We find mean offsets of  $\lesssim 0.3$  mag up to  $250\mu\text{m}$  with most fields/filters agreeing within  $< 0.15$  mag. The text in each panel corresponds to the mean offset measured above the flux uncertainty depth (dashed line, or dotted if present). The  $350\mu\text{m}$  3D-Herschel photometry is notably brighter (mean offsets of  $\sim 0.03$  up to 1 mag), likely due to the shallow depth of this band and the different methods of flux extraction between catalogs. Despite the offsets in the SPIRE350 fluxes, the boosted errors in this band typically exceed the systematic offset, allowing the fits to account for these variations and appropriately weight the photometry.

Second, galaxy counts of the 3D-Herschel photometric catalogs are presented in Figure 2 to demonstrate that photometric estimations were consistent across all fields. The 3D-Herschel fields are all in agreement, with minor variations at the peak owing mainly to field-to-field variations in the depth of the FIR imaging. Now with validated 3D-Herschel photometric catalogs, SED modeling from `Prospector` using the long-wavelength combined catalogs can be completed as described next.

#### 4. SED MODELING

We use the most recent and flexible version, `Prospector- $\beta$` , as the baseline of our SED modeling (Wang et al. 2023). This 17-parameter framework incorporates a nonparametric SFH, two-component dust attenuation, and variable dust emission, enabling a more complete treatment of galaxy physics than earlier 14-parameter implementations such as `Prospector- $\alpha$`  used by Leja et al. (2019b). To make the analysis computationally feasible for our large sample, we rely on an emulator – a neural network trained to reproduce full `Prospector` outputs – rather than recalculating spectra at each MCMC step. The extended list of pa-

parameters and their priors included in the emulator are listed in Table 1 of Mathews et al. (2023). The emulator yields nearly identical posterior distributions for most parameters, but at a fraction of the computational cost, allowing the four fields to be modeled within weeks, as each object requires on average 10 minutes of compute time.

For continuity with past work, Section 4.1 first benchmarks the emulator against the simpler `Prospector- $\alpha$`  framework applied to the 3D-HST catalog, before turning to our new 17-parameter modeling of the 3D-Herschel dataset in Section 4.2.

#### 4.1. 3D-HST modeling fits

The full `Prospector` SED modeling code has been employed to fit the 3D-HST photometric catalogs (0.3 - 24 $\mu$ m), which serve as our baseline comparisons. When modeling the IR emission, `Prospector` assumes energy balance by having dust attenuated in the UV-NIR re-emitted as IR radiation (Da Cunha et al. 2008), and the shape of the IR SED is defined by dust emission templates provided by Draine & Li (2007). To address the lack of observational constraints in the FIR, the IR SED (rest-frame  $\sim$ 4-1000 $\mu$ m) is fixed such that the conversion from Spitzer/MIPS 24 $\mu$ m to total IR Luminosity ( $L_{\text{IR}}$ , calculated from 8-1000 $\mu$ m) approximates the log-average of the Dale & Helou (2002) templates, as described by Wuyts et al. (2008). For the UV-MIR fits, the three dust emission parameters defined by the Draine & Li (2007) models,  $q_{\text{PAH}}$ ,  $U_{\text{min}}$ , and  $\gamma$  are fixed to 2, 1, and 0.01, respectively.

The earlier fits presented in Leja et al. (2019b) involve subtle variations in the treatment of the 3D-HST photometric catalog as compared to this work. During the assembly of the 3D-HST catalogs, as detailed in Skelton et al. (2014), corrections to the zero-points were derived for each instrument and filter to optimize the absolute flux calibration. In lieu of applying these corrections, Leja et al. (2019b) instead inflated the flux errors by the equivalent amount for each photometric band, except for the space-based bands (HST and Spitzer), which inherently possess more stable zero-points. Instead, we leave the zero-point corrections as originally applied for the SED modeling and thus adopt the 3D-HST photometric catalogs wholesale. We refer the reader to Mathews et al. (2023) for a detailed comparison of the emulator results for the exact same 3D-HST photometric input.

In order to test for the impact of this change in approach relative to Leja et al. (2019b), while also staying economical, we re-run the emulator on a subset of sources. Figure 3 shows comparisons for six posterior medians for 1,000 randomly selected galaxies evenly dis-

tributed between the four fields, as presented in Leja et al. (2019b) (x-axis), to the emulation fits of the publicly released 3D-HST catalog (y-axis). We find no statistical difference in the inferred physical parameters within their quoted uncertainties; mean offsets are less than 0.1 dex for all presented parameters in Figure 3.

#### 4.2. 3D-Herschel emulation fits

To accommodate FIR SED modeling, we adopt slight modifications to the `Prospector` framework following Mathews et al. (2023). In particular, the emulator now allows the three thermal dust emission parameters of Draine & Li (2007) – previously fixed in fits without FIR constraints (Section 4.1) – to vary. These free parameters are the PAH mass fraction ( $q_{\text{PAH}}$ ), the minimum diffuse ISM radiation field strength heating the dust ( $U_{\text{min}}$ ), where  $U$  is a dimensionless scaling factor, and the fraction of starlight ( $\gamma$ ) exposed to radiation field strengths  $U$  between  $U_{\text{min}}$  and  $U_{\text{max}}$ , which we fix to  $U_{\text{max}} = 10^6$ .

Together with the 14 parameters of the baseline model and a fixed, galaxy-dependent redshift input, our physical model spans 17 parameters in total. Details of the prior distributions and emulator validation are provided in Mathews et al. (2023), who also verify that the emulator shows no apparent bias and recovers posterior medians consistent with traditional SPS codes. This gives us confidence in using the emulator for this study, especially since modeling  $\sim$ 41,000 galaxies demands the  $10^3$ – $10^4$  speed-up in runtime it provides.

#### 4.3. Sample selection

Within the four CANDELS fields we focus on herein, there are 166,767 sources in the catalog, whereas we focus hereafter on comparing results from Leja et al. (2019b, 2022) and thus model a subset of 41,387 galaxies. We adopt the 90% stellar mass completeness limits following Tal et al. (2014), as listed in Table 5 along with the number of sources for each redshift range and the corresponding redshift type, leaving us with a mass-complete sample of 34,443 galaxies.

## 5. STELLAR POPULATION SYNTHESIS MODELING

Using the UV-FIR photometry from the 3D-Herschel photometric catalogs, `Prospector` models the SED and infers the stellar parameters of each galaxy within a Bayesian framework. For each of the 17 free parameters, we adopt the median of the posterior distribution as the best estimate, with uncertainties given by the 16th and 84th percentiles.

**Table 5.** Corresponding redshifts in their respective ranges with stellar mass limits

Redshift Range	Completeness Limit [ $\log(M_\star/M_\odot)$ ]	# Spectroscopic	# Grism	# Photometric
$0.5 < z < 0.8$	8	955	2,297	5,778
$0.8 < z < 1.2$	8.5	822	2,930	6,660
$1.2 < z < 1.8$	9	359	3,193	6,314
$1.8 < z < 2.5$	9.4	135	1,600	3,400
Total:		6.6%	29.1%	64.3%

From the 17 physical parameters inferred from `Prospector`, we focus on a subset most likely to be affected by adding FIR constraints: star formation rate (SFR), surviving stellar mass ( $M_\star$ ), diffuse and birth-cloud optical depths ( $\tau_{\text{diffuse}}$ ,  $\tau_{\text{birthcloud}}$ ), the slope of the attenuation law ( $\tau_{\text{index}}$ ), stellar age, and stellar metallicity. Notably, `Prospector` reports the surviving stellar mass, accounting for stellar mass loss from evolutionary processes (e.g., asymptotic giant branch (AGB) winds, supernovae), rather than the total mass formed. Throughout, ‘stellar mass’ refers to this surviving mass.

We examine offsets in the inferred SPS parameters between fits that include Herschel photometry versus those using photometry only up to  $24\mu\text{m}$  in Figure 4. Our goal is to identify the galaxy properties most affected by the addition of FIR constraints. Figure 4 presents the offset for several key stellar parameters as a combination of histograms and scatter plots. At the top of each column, a histogram shows the distribution of offsets for the corresponding parameter along the x-axis. Additionally, the histogram of offsets in the star formation rates appears at the right end of the bottom row.

Overall, the parameters do not exhibit systematic offsets under the new modeling constraints; most histograms are centered around  $\Delta = 0$  (red line). The inferred ages are an exception, showing a tendency toward older ages, though a majority ( $\sim 73\%$ ) of the sample remains within the  $1\sigma$  uncertainty.

In each scatter subplot of Figure 4, the  $1\sigma$  uncertainty box is outlined, corresponding to the median upper and lower  $1\sigma$  uncertainty of the respective parameter along that axis. The individual  $1\sigma$  uncertainties are calculated by computing the distance between the median 84th and 50th percentile values for the upper uncertainty, and the median 50th and 16th percentile values for the lower uncertainty. The 84th, 50th, and 16th percentile values are taken from the fits with no Herschel photometry.

The blue box in the upper left corner of each subplot in Figure 4 shows the percentage of the population within the  $1\sigma$  region, indicating that most objects (55-69%) deviate by less than  $1\sigma$  for the selected proper-

ties. However, the outliers show clear correlations when FIR constraints are added: dust attenuation ( $\tau_{\text{diffuse}}$  and  $\tau_{\text{birthcloud}}$ ) increases with higher SFRs and decreases stellar age. Based on these initial results, adding Herschel photometry does not introduce significant systematic offsets in the median inferences of key properties. Importantly, the inferred star-forming main sequence (SFMS) estimated from our sample of 34,443 objects is not systematically offset and remains in agreement with the previous fits presented in [Leja et al. \(2022\)](#), showing an average deviation in the median (ridge) SFR of  $0.1 \pm 0.07$  dex and no greater than  $\sim 0.25$  dex for a fixed stellar mass. We defer a more in-depth discussion of the SFMS to Section 6.2.

Herschel imaging is intrinsically low-resolution, and even after the deblending, a majority of measurements in our mass-limited sample are upper limits ( $\gtrsim 90\%$ ). Nevertheless, these upper limits still provide meaningful constraints in the modeling. For example, at low signal-to-noise (SNR  $\approx 1$  for all 100, 160, 250, and  $350\mu\text{m}$  observations), the median uncertainties in  $\log(\text{SFR})$ ,  $\log(Z/Z_\odot)$ , and  $\tau_{\text{diffuse}}$  are reduced by 0.06, 0.09, and 0.08 dex, respectively, relative to fits without Herschel photometry.

However, to enable a more robust assessment, a high-quality sample of Herschel detections is required. In particular, such a sample is needed to quantify how reliably  $24\mu\text{m}$  photometry traces the IR luminosity ( $L_{\text{IR}}$ ) and the stellar parameters dependent on  $L_{\text{IR}}$ .

## 6. CHANGES IN INFERRED PARAMETERS FOR GALAXIES WITH SIGNIFICANT HERSCHEL DETECTIONS

To construct an optimal sample of galaxies that are both well-imaged by Herschel and most likely to be affected by the new FIR constraints (i.e., IR-bright, typically meaning highly star-forming), we select sources with  $\text{SNR} \geq 3$  and a ‘use’ flag of 1 in at least two Herschel bands (PACS100, PACS160, SPIRE250, and

**Table 6.** Percent of IR-bright sample in mass bins

Mass Range [ $\log(M_*/M_\odot)$ ]	Number of Galaxies	Percent of Mass-Limited Population
$9.0 \leq \log(M_*/M_\odot) < 9.75$	17	0.12%
$9.75 \leq \log(M_*/M_\odot) < 10.5$	384	4.43%
$10.5 \leq \log(M_*/M_\odot) < 11.25$	653	16.80%
$11.25 \leq \log(M_*/M_\odot)$	64	21.33%

SPIRE350) In addition, we require a MIPS  $24\mu\text{m}$  detection ( $\text{SNR} \geq 3$ ), since the previous fits relied on the observed-frame  $24\mu\text{m}$  flux as a proxy for the FIR.

Approximately 33% of this population exhibit poor-fitting FIR SEDs, often due to bright interlopers contaminating the photometry of low-mass galaxies and producing overestimated fluxes in either PACS100 or PACS160. To remove these cases, we require  $\chi^2 < 3$  in both PACS100 and PACS160 when comparing model fluxes to the deblended photometry. The final IR-bright sample consists of 1118 objects. The fractional contribution of the IR-bright population to the total sample, as a function of stellar mass, is listed in Table 6. Figure 5 shows the composite SEDs of this sample inferred from fits including Herschel photometry (blue) and from fits without Herschel (purple).

To construct the composite, each SED is normalized by the average flux at rest-frame  $1\mu\text{m}$  from the best-fit spectrum excluding Herschel photometry, and the median spectrum is then calculated. The composites are supported by Herschel observations at 70, 100, 160, 250, and  $350\mu\text{m}$  as well as HST and Spitzer photometry from the 3D-HST photometric catalogs. For each object, the photometry is shifted to the rest frame, and median values are plotted as large X's, with standard deviations shown for filters in which fewer than 50% of the data are upper limits. The fraction of upper limits in each Herschel filter is indicated in the top right corner, and for bands with more than 50% upper limits, the limits are taken as three times the error and plotted as downward-pointing triangles.

The composite SEDs are overplotted with the  $z=1$  star-forming template from Kirkpatrick et al. (2012). The FIR spectrum of the 3D-Herschel IR-bright composite closely follows the shape of this template, in contrast to the fits without Herschel data, underscoring the robustness of our high-quality sample. We present this sample in greater detail, along with its placement on the SFMS, in the following section.

### 6.1. Age-dust-metallicity degeneracy

Dust attenuation is inferred from UV-optical-NIR starlight, and in the absence of FIR measurements, `Prospector` estimates the re-radiated dust emission by assuming energy balance. Extending photometric constraints into the FIR with Herschel are therefore critical for improving obscured SFR and related  $\tau$  estimates, thus reducing degeneracies. These degeneracies arise from uncertainties in dust attenuation, which propagate into stellar age and metallicity estimates, since all three parameters redden the UV/optical SED. Figure 6 illustrates the effect by showing offsets in the mass-weighted age, optical depth of diffuse dust, and stellar metallicity as a function of the offsets in the SFR (top row) and stellar mass (bottom row).

We separate the sample into two sub-populations: objects with higher diffuse dust attenuation and star formation (red) and those with lower values (purple) in their updated estimates, reflecting the critical role of Herschel data in reducing uncertainties in obscured SFR and  $\tau_{\text{diffuse}}$ . To evaluate the significance of the offsets beyond the  $1\sigma$  box, we include only objects whose updated uncertainties fall outside the range of their previous estimates. The fraction of each sub-population located in a given quadrant is reported in the corresponding corner, while the percentage within the  $1\sigma$  box is indicated in the respective colored box.

Relative to the mass-complete sample – in which  $24\mu\text{m}$  serves as a robust proxy for FIR dust emission (with  $>60\%$  of objects contained within the  $1\sigma$  box; Figure 4) – a smaller fraction of the IR-bright sample falls within  $1\sigma$  ( $\sim 40\%$  -  $60\%$  for  $\tau$ , SFR,  $M_*$ , and age). The offsets shown in Figure 6 do not indicate substantial systematic biases in dust estimates based on MIR analogs: 90 objects are inferred to be significantly dustier and more star-forming, while 95 are less dusty and less star-forming, together comprising  $\sim 8\%$  of the IR-bright sample.

The  $1\sigma$  boxes in Figure 6 provide a visual summary of the typical uncertainties in the baseline catalog and help visualize how the offsets correlate, but they do not robustly quantify the significance of the differences on an object-by-object basis. Here, we compute the

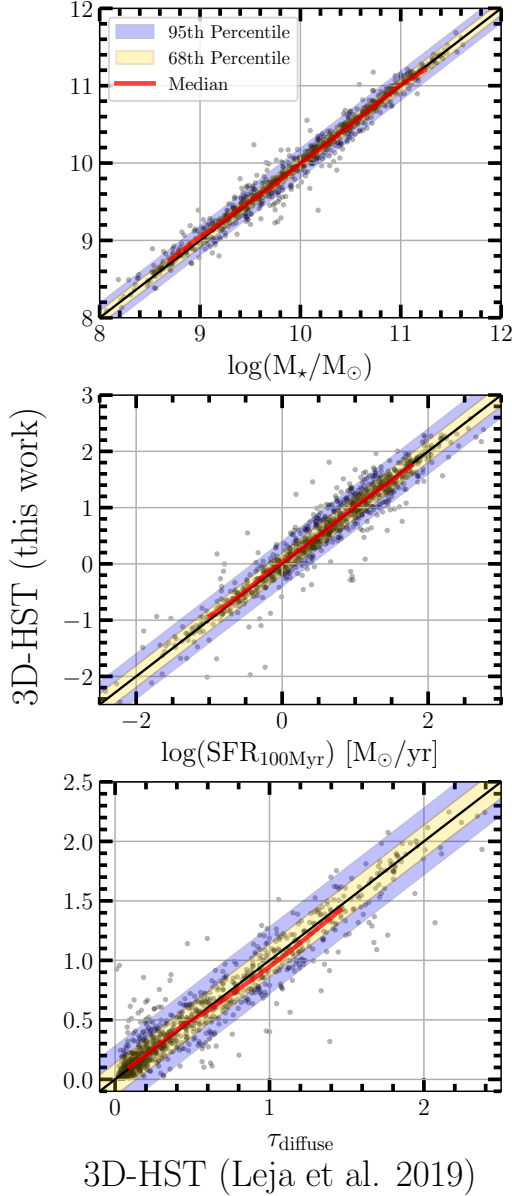


**Figure 3.** Comparison of posterior medians inferred from full Prospector fits of the adjusted 3D-HST catalog (Leja et al. 2019b; x-axis) versus our Prospector emulation on the publicly released 3D-HST catalog (y-axis). Panels show (a) stellar mass, (b) diffuse-dust attenuation, (c) stellar metallicity, (d) dust index, (e) SFR, and (f) mass-weighted age. The one-to-one line is in black and red lines show median offsets. The emulator reproduces direct-fit estimates within their statistical uncertainties.

uncertainty-normalized residuals for each source,

$$\frac{\Delta x}{\sigma_{\Delta x}} = \frac{x_H - x_{\text{noH}}}{\sqrt{\sigma_H^2 + \sigma_{\text{noH}}^2}} \quad (1)$$

where the subscripts H and noH denote values obtained with and without Herschel constraints. We find

that stellar mass, SFR, and  $\tau_{\text{diffuse}}$  exhibit substantial tension: 43% of galaxies have  $|\frac{\Delta x}{\sigma_{\Delta x}}| > 1$  and 15% have  $|\frac{\Delta x}{\sigma_{\Delta x}}| > 2$ , exceeding Gaussian expectations. In contrast, age,  $\tau_{\text{birthcloud}}$ , and metallicity, show a fewer percent of large residuals, more consistent with Gaussian-distributed uncertainties.

By directly constraining obscured SFR and dust emission, we obtain more reliable estimates of the degenerate parameters. Consequently, dustier, more star-forming systems are inferred to have younger ages, lower stellar masses, and reduced metallicities, while the opposite holds for less dusty and star-forming galaxies. Many of the offsets outside the  $1\sigma$  box are driven by  $\tau_{\text{diffuse}}$ , likely reflecting the limitations of earlier  $\tau$  estimates derived from models lacking FIR data. In the absence of FIR constraints, a fixed FIR color was used to match the log-averaged Dale & Helou (2002) templates, which either over- or underestimates the dust content in more than half of the IR-bright sample.

To highlight the limitations of fixed SED templates used in fits without FIR constraints, Figure 7 presents composite SEDs for the IR-bright sample: objects whose offsets remain within  $1\sigma$  (left panel) and those that are significantly dustier and more star-forming (right panel). These composites are constructed following the same procedure as in Figure 5, as described in Section 6.

For objects where modeling up to the MIR was sufficient to estimate dust content and obscured star formation (left panel), the FIR shapes of the two fits nonetheless differ. Incorporating Herschel constraints allows the FIR spectrum to vary freely, producing dust bumps that consistently peak at shorter wavelengths than in the previous fits. This trend also holds for the dustier, more star-forming systems shown in the right panel. The FIR dust bump is set by three dust emission parameters treated as free in our modeling, each directly linked to the emitting dust temperature. The implications of fixing these parameters are discussed in Section 7. Despite systematic differences in the FIR dust bump shape and consistently warmer peaks in the left panel, the total IR luminosity (3-1100 $\mu\text{m}$ ) is not affected, consistent with the SFR and dust attenuation offsets of these objects.

In the right panel of Figure 7, the Herschel-informed composite SED exhibits substantially greater FIR emission than the fits that underestimated  $\tau_{\text{diffuse}}$  and SFR. For these 90 objects alone, the calculated  $L_{\text{IR}}$  is  $0.3 \pm 0.25$  dex greater in models inferred with Herschel FIR photometry. Because FIR flux, and by extension IR luminosity, is a key proxy for the obscured SFR – which dominates the star formation budget above  $\log(M_*/M_\odot) \sim 9.4$  (Whitaker et al. 2017) – this difference is significant. Although a comparable number of

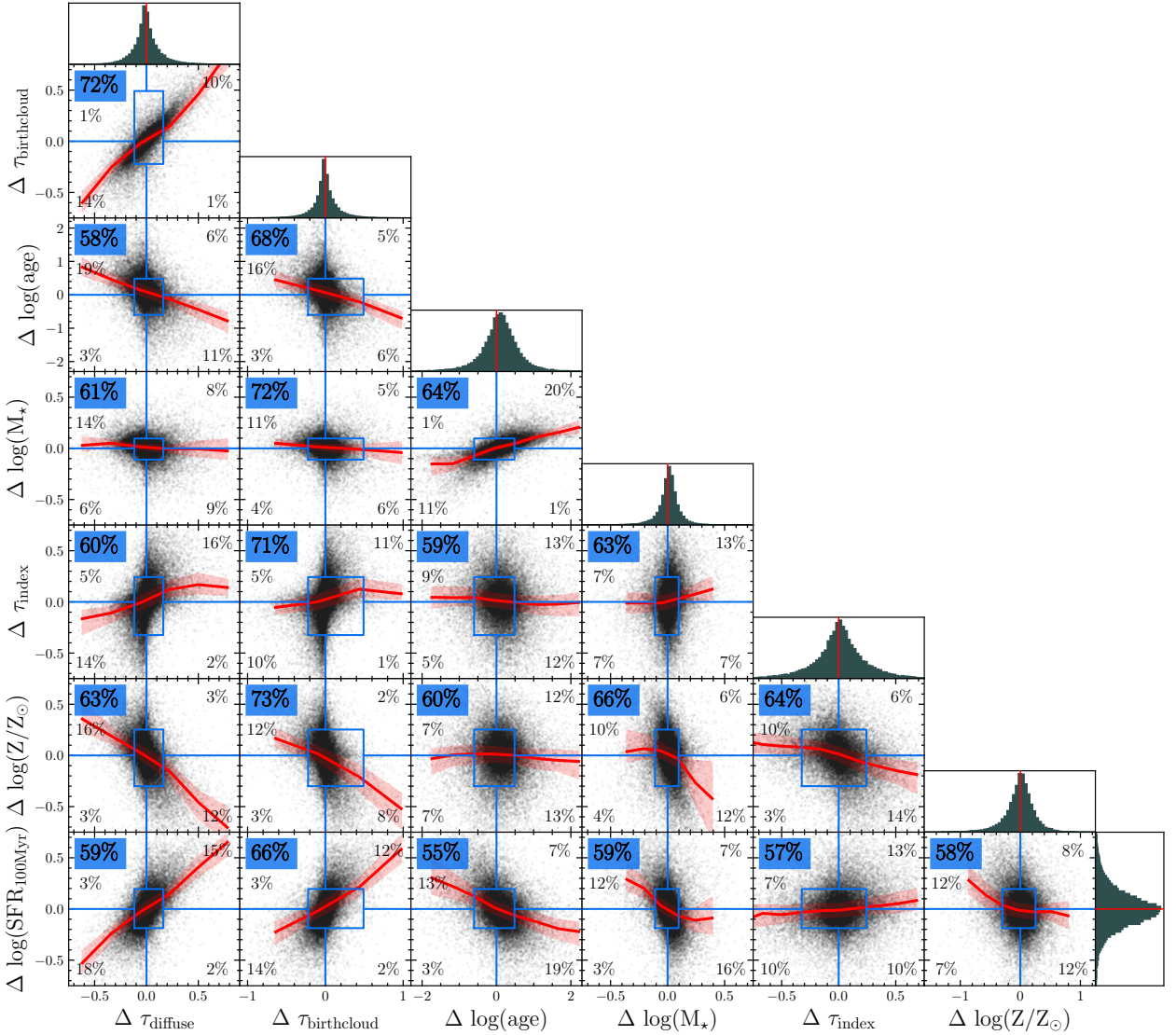


**Figure 4.** Comparisons of fits with and without Herschel photometry, showing offsets (with - without Herschel) in 7 out of 17 of the inferred stellar parameters plotted against each other. Histograms of the offsets are shown above each column and at the end of the last row. Parameters (left to right, bottom row): diffuse dust attenuation ( $\tau_{\text{diffuse}}$ ), birth cloud dust attenuation ( $\tau_{\text{birthcloud}}$ ), mass-weighted age, stellar mass, diffuse dust index ( $\tau_{\text{index}}$ ), stellar metallicity, and SFR over the last 100 Myr bin (y-axis of bottom row). Blue boxes indicate the percent within  $1\sigma$ , based on UV-MIR modeling; other indicated percentages refer to the population in the respective quadrant, excluding the  $1\sigma$  box.

objects show increases and decreases in SFR, the SFMS provides a more meaningful framework for evaluating how the IR-bright population is affecting well-studied scaling relations.

### 6.2. Star-Forming Main Sequence

One of the most robustly measured relations in galaxy evolution is the SFMS: the tight correlation between stellar mass and SFR that traces where typical galaxies form the bulk of their mass, first identified by Noeske

et al. (2007). The existence of this relation indicates that most star-forming galaxies grow in a relatively steady fashion rather than through stochastic bursts, at least out to  $z \sim 3$ . Given its central role in our understanding of galaxy growth, the SFMS has been characterized across a wide redshift range and with diverse methodologies (e.g., see synthesis in Speagle et al. 2014), yielding variations in its slope and normalization (e.g., Elbaz et al. 2007; Daddi et al. 2007) as well as scatter (Whitaker et al. 2012; Speagle et al. 2014; Schreiber

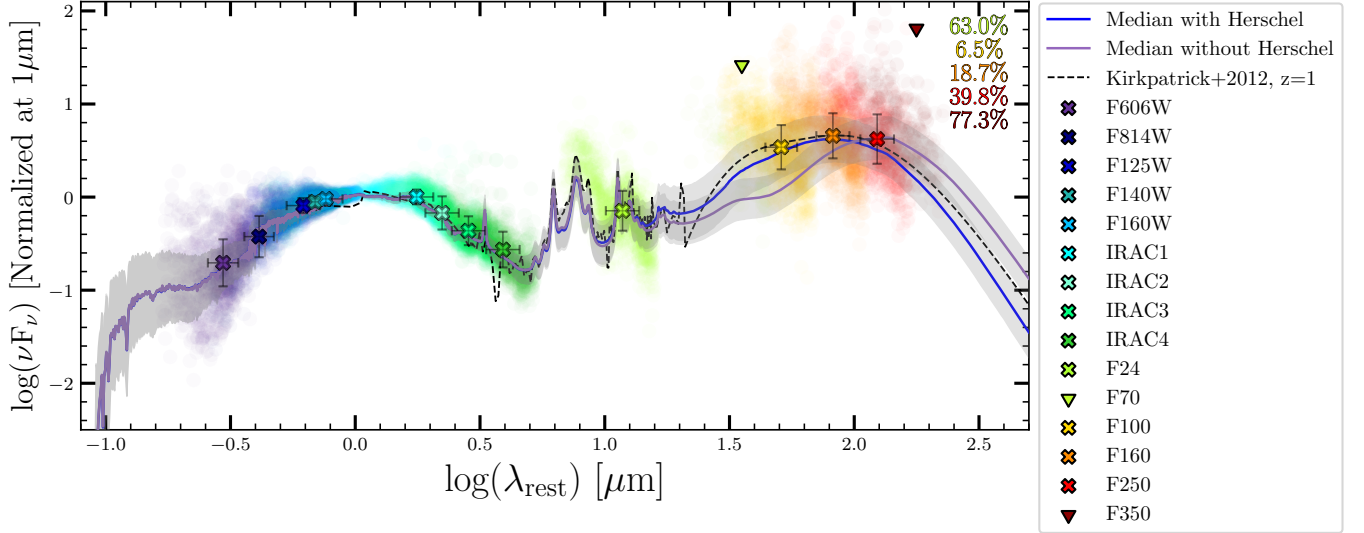


**Figure 5.** Composite SEDs of the IR-bright sample from `Prospector` fits adding Herschel FIR photometry to the UV to MIR 3D-HST photometry (blue line), compared to fits without Herschel (purple line) and the  $z \sim 1$  star-forming template of Kirkpatrick et al. (2012) (dashed line). Crosses represent median photometry of the individual measurements (all SNR > 3 detections plotted as circles), whereas inverted triangles represent the median upper limits for cases where >50% of Herschel detections have SNR < 3. The percentage of upper limits in each Herschel band is listed in the upper right. Redshifts range from 0.5-2.5, with 294 of the 1118 sources having spectroscopic redshifts.

et al. 2018). Later work revealed that the relation is not strictly linear: at high masses, the sequence flattens, introducing curvature (Whitaker et al. 2014; Lee et al. 2015).

While subsequent studies have continued to refine measurements of the SFMS (e.g., Abramson et al. 2015; Schreiber et al. 2015; Tomczak et al. 2016; Kurczynski et al. 2016; Popesso et al. 2019; Boogaard et al. 2018), observations have generally shown a persistent  $\sim 0.3$  dex offset towards higher SFRs relative to predictions from cosmological simulations (Furlong et al. 2015; Davé et al. 2019; Nelson et al. 2021). Leja et al. (2022) recently reconciled this discrepancy using the same 3D-HST photometric catalogs employed in previous works (e.g., Whitaker et al. 2014), but with more sophisticated SPS modeling. Nonetheless, in the absence of direct FIR constraints, uncertainties in the underlying modeling assumptions remain.

In Figure 8, we show the SFMS for our full sample of 34,443 galaxies, comparing `Prospector` fits that include Herschel photometry (red) to those using UV-MIR data (blue). The SFRs from `Prospector` are averaged over the most recent 100 Myr, rather than the instantaneous values, consistent with the timescale probed by UV+IR SFR indicators. We define the SFMS by its mode, or *ridgeline*, following recent efforts to avoid the need for explicit quiescent/star-forming separation. The mode more accurately identifies where most star formation occurs, appearing as the steep ridge on a contour

map, while largely excluding quenched galaxies (Renzini & Peng 2015). Leja et al. (2022) estimated the ridgeline as the density peak in the SFR-mass plane using a flexible neural network (a normalizing flow). In this work, however, we adopt a similar but robust approach by directly estimating the mode by first discretizing the continuous values to the nearest 0.1, effectively computing the histogram mode with a bin width of 0.1.

The SFMS derived from Herschel-constrained fits and that recovered from UV-MIR-only ( $\leq 24 \mu\text{m}$ ) fits coincide closely and are not systematically offset across redshift bins, differing by  $\sim 0.1$  dex on average (and no more than 0.25 dex in any stellar mass bin). This agreement demonstrates that rest-MIR photometry alone can robustly recover galaxy SFRs across a wide range of properties. In Figure 8, the IR-bright population is color-coded according to whether objects became significantly dustier and more star-forming (red), less dusty/star-forming (purple), or largely unchanged (black), as defined in Figure 6. The bottom row shows the difference in the SFR between the two sequences (Herschel - UV-MIR) as a function of the stellar mass inferred from the FIR-constrained modeling.

Adding FIR data does not substantially change the overall SFMS of IR-bright objects, although catastrophic under- or over-estimations of SFRs occasionally occur for individual cases, with offsets reaching up to an order of magnitude. Galaxies that became dustier and more star-forming in the updated modeling (red) exhibit

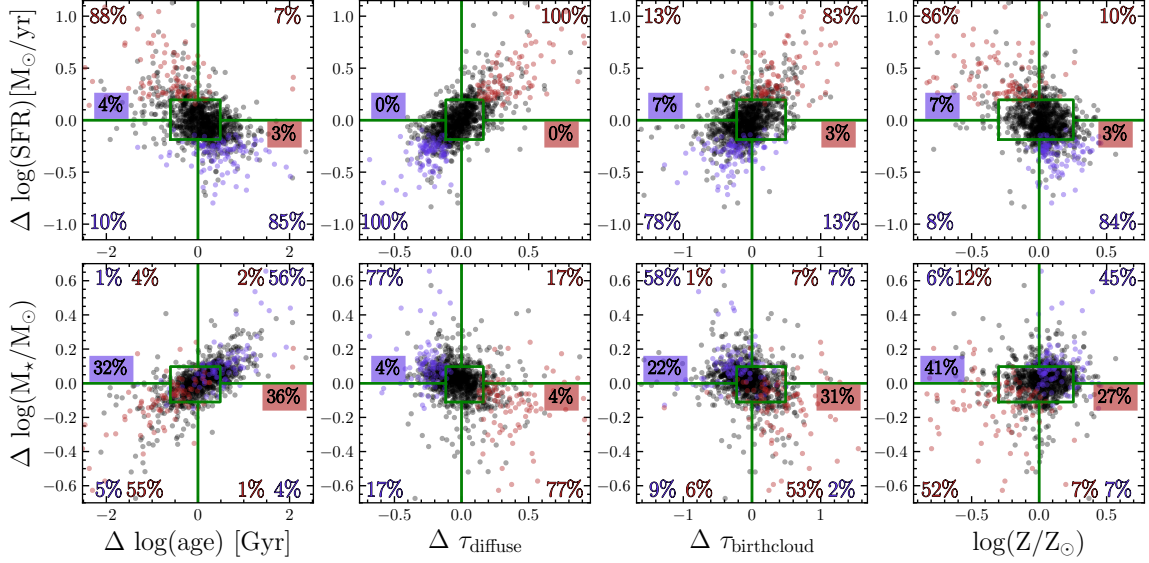


**Figure 6.** Offsets (with - without Herschel) in star formation rate (top row) and stellar mass (bottom row) as a function of mass-weighted age, diffuse dust, birthcloud dust, and stellar metallicity (left to right). Objects are color-coded as dustier and more star-forming (red) or less dusty and less star-forming (purple). IR-bright galaxies modeled without FIR constraints are more poorly inferred than the full sample; the more dust-obscured, star-forming objects tend to be younger and more massive, while the less dusty population shows the opposite trend. Percentages of each subpopulation in each quadrant is reported in the corresponding color and corner, while the percentage within the  $1\sigma$  box is indicated in the colored text box.

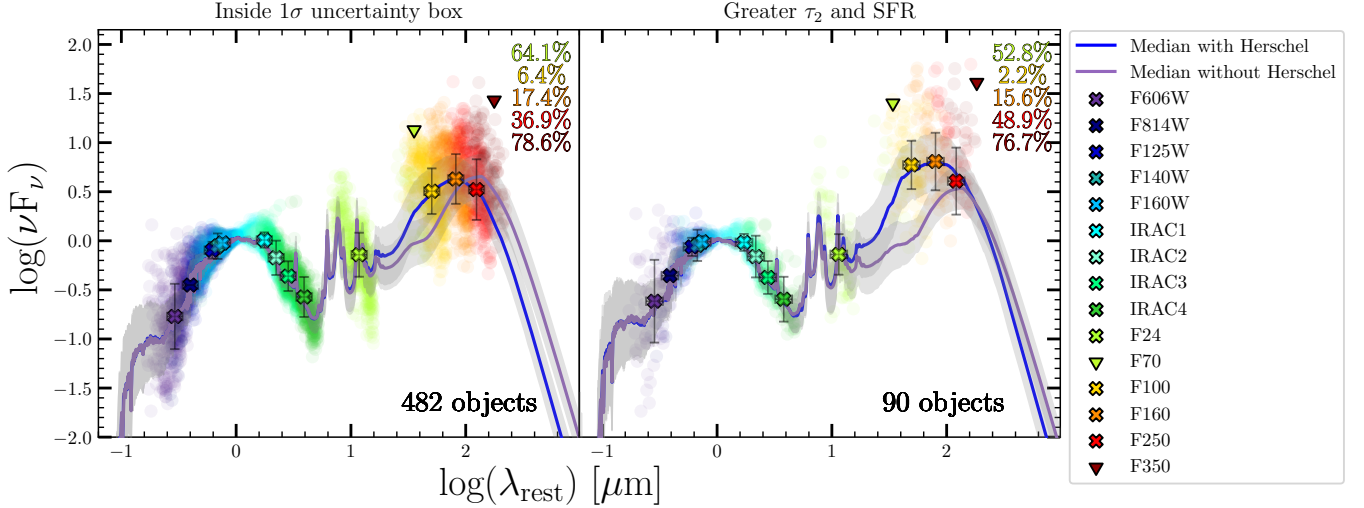


**Figure 7.** Composite SEDs with (blue) and without Herschel photometry (purple), normalized at  $1\mu\text{m}$ . The composites in the left panel are constructed from sources with diffuse dust and SFR offsets within their original  $1\sigma$  uncertainties, while the right panel is created from IR-bright objects that are significantly dustier and more star-forming under the new constraints. The percent of upper limits in each Herschel band is listed in the top right.

the largest discrepancies relative to the less dusty, less star-forming population (purple). Some objects with underestimated SFRs were previously inferred to lie in the green valley or near the quiescent population, while those with overestimated SFRs were often placed among the most actively star-forming galaxies in their mass bin. Between  $0.5 < z < 1.5$ , underestimates are more com-

mon at lower stellar masses, whereas overestimates are more frequently associated with higher-mass galaxies.

Nevertheless, MIR-limited fits recover the SFRs of the best Herschel-detected, FIR-bright galaxies with reasonable accuracy:  $\sim 70\%$  of the IR-bright sample fall within  $1\sigma$  of the one-to-one relation. The remaining outliers underscore the limitations of estimating the full IR lu-

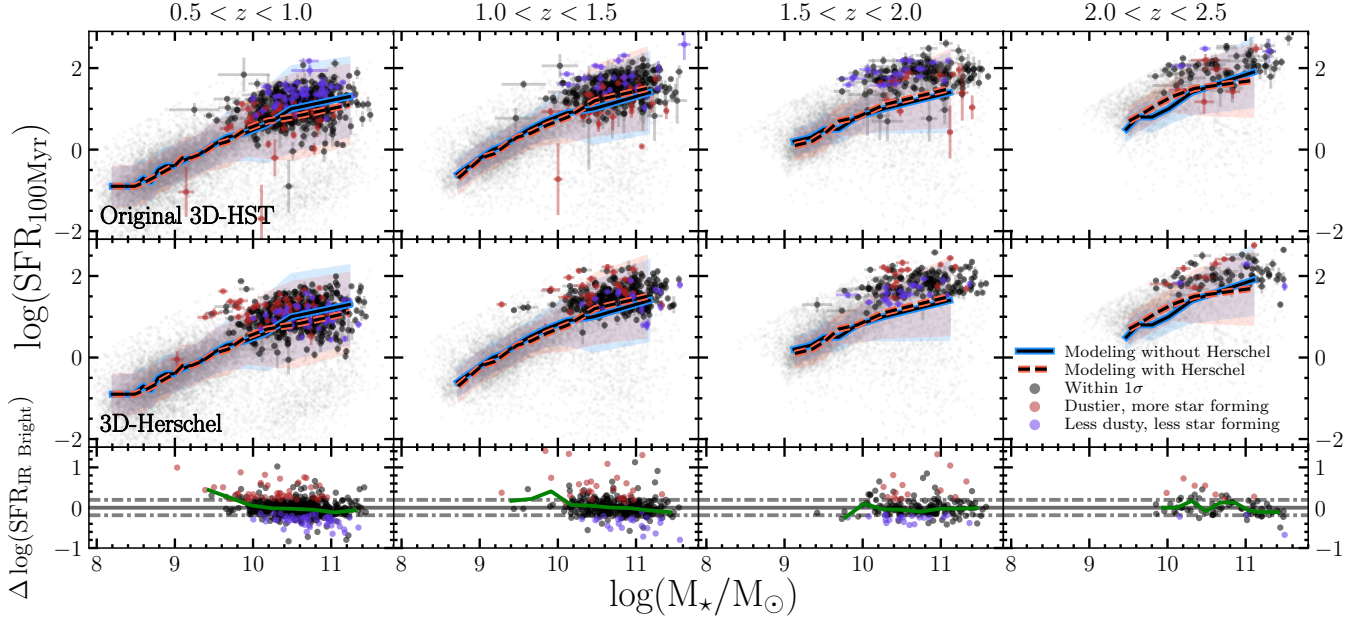


**Figure 8.** IR-bright population (circles) overplotted on the SFMS of the mass-limited sample, inferred from UV-MIR fits (blue line) and from Herschel-constrained fits (red dashed line). The top row shows SFRs and stellar masses from UV-MIR fits, whereas the middle row shows the same population from UV-FIR fits, and the bottom row shows SFR differences between the two sequences (Herschel – UV-MIR). Objects are color-coded as in Figure 6: significantly dustier and more star-forming (red) or less dusty and less star-forming (purple).

minosity from UV-MIR data with fixed templates alone, as discussed further in Section 6.3.

### 6.3. $F_{\text{TIR}}$ and $F_{7.7}$

The total integrated IR luminosity,  $L_{\text{IR}}$ , measures the bolometric output of dust and is obtained by integrating over the IR spectrum (Sanders & Mirabel 1996). Previous studies have frequently used  $24\mu\text{m}$  flux as a proxy for estimating  $L_{\text{IR}}$  (e.g., Wuyts et al. 2008; Whitaker et al. 2012, 2014). The Spitzer/MIPS  $24\mu\text{m}$  band captures emission from the prominent  $7.7\mu\text{m}$  polycyclic aromatic hydrocarbon (PAH) feature at redshifts of  $\sim 1-3$  (Rieke et al. 2004). With appropriate SED templates, this feature can be used to estimate FIR emission through established conversions between PAH strength and total dust mass, making it a practical tracer of dust-obscured luminosity during cosmic noon, and, by extension, the obscured SFR (Calzetti et al. 2007; Kennicutt et al. 2009; Kennicutt & Evans 2012; Rujopakarn et al. 2013).

In our analysis, the `Prospector` fitting code adopts the dust emission models of Draine & Li (2007) to define the IR SED. By contrast, MIR-only conversions to  $L_{\text{IR}}$  typically rely on a single log-averaged IR template from Dale & Helou (2002) (e.g., Whitaker et al. 2014). To reduce template-dependent effects when analyzing the same underlying data set, Leja et al. (2022) fixed the Draine & Li (2007) templates to reproduce the  $L_8$  to

$L_{\text{IR}}$  color of the Dale & Helou (2002) templates, whereas we relax this constraint when incorporating FIR data.

While  $24\mu\text{m}$  photometry has long been used as a proxy for estimating  $L_{\text{IR}}$ , recent studies have begun to probe the robustness of this approach with higher-fidelity data. Studies of the relationship between the total IR luminosity to MIR luminosity have found that the ratio  $L_{\text{IR}}/L_8$  remains approximately constant up to  $z \approx 2.5$  (Elbaz et al. 2011; Reddy et al. 2011). More recently, however, Shivaie et al. (2024) used the Mid-Infrared Instrument (MIRI; Rieke et al. 2015; Wright et al. 2023) on the James Webb Space Telescope (JWST; Gardner et al. 2023), Shivaie et al. (2024) to show that the strength of the  $7.7\mu\text{m}$  PAH feature is strongly correlated with stellar mass. To place our analysis in the context of this high-quality JWST study, we calculate integrated IR and  $7.7\mu\text{m}$  fluxes for direct comparison with Shivaie et al. (2024).

We derive the total IR power ( $F_{\text{TIR}}$ ) by integrating the best-fit SED over the range  $3-110\mu\text{m}$  ( $\int F_\lambda d\lambda$ ). The integrated flux of the  $7.7\mu\text{m}$  PAH feature ( $F_{7.7}$ ) is calculated following the methodology of Draine et al. (2021). To isolate the PAH emission from the underlying warm dust continuum, we define a ‘clipped’ flux by selecting anchor points on either side of the feature where the PAH emission begins. At the edge wavelengths ( $6.9$  and  $9.7\mu\text{m}$  for the  $7.7\mu\text{m}$  feature), the flux is set to zero, and

a ‘clip line’ ( $F_\lambda$ ) is drawn between them. The clipped flux for the  $7.7\mu\text{m}$  feature is then defined as:

$$F_{\text{clip}}(\text{band}) \equiv \int_{6.9\mu\text{m}}^{9.7\mu\text{m}} (F_\lambda - F_\lambda^{(c.l.)}) d\lambda. \quad (2)$$

Visualizations of the regions used to calculate  $F_{\text{TIR}}$  and  $F_{7.7}$  are shown in Figure 10.

We present our estimates of  $F_{\text{TIR}}$  and  $F_{7.7}$  for the IR-bright sample in Figure 9, showing the ratio of the two as a function of stellar mass and color-coded by  $q_{\text{PAH}}$ . The parameter  $q_{\text{PAH}}$  denotes the fraction of total dust mass in PAHs, serving as an analog to the MIR-to-IR ratio. For context, we also plot the median relations for the IR-bright sample modeled without Herschel photometry and for the full 3D-Herschel star-forming population, with quiescent galaxies removed using a UVJ cut following Schreiber et al. (2015) and excluding galaxies with specific star formation rates (sSFR,  $\text{SFR}/M_*$ )  $< 10^{-10}\text{yr}^{-1}$ ). This sample cut follows Shivaie et al. (2024), allowing our study to be placed in context with theirs.

The Herschel FIR constraints indicate that our previous fits, based on a fixed IR SED and a non-evolving  $F_{\text{TIR}}/F_{7.7}$  ratio, underestimate the total IR emission at stellar masses  $< 10^{10.4}M_\odot$ . At the highest masses, the ratio approaches unity. However, we interpret this trend with caution: Elbaz et al. (2011) identified a tail of high  $L_{\text{IR}}/L_8$  ratios associated with compact projected star formation densities, characteristic of galaxies in a starburst mode. The increased ‘compactness’ of such systems produces more intense radiation fields, leading to PAH destruction and elevated  $L_{\text{IR}}/L_8$  values.

Elbaz et al. (2011) quantified starburst intensity using the excess of the specific SFR (i.e., the rate of growth of stellar mass per unit existing stellar mass, with  $\text{sSFR} \equiv \text{SFR}/M_*$ ) for a galaxy, labeled as ‘starburstiness’ ( $R_{\text{SB}}$ ), defined by:

$$R_{\text{SB}} = s\text{SFR}/s\text{SFR}_{\text{MS}} \quad (3)$$

where  $s\text{SFR}_{\text{MS}}$  is the equivalent value for a galaxy of the same stellar mass residing on the SFMS for a given redshift. Galaxies are considered to be in a starburst mode when  $R_{\text{MS}} > 2$ . To assess the role of starburst in our sample, we flag these objects and display them as stars in Figure 9. Based on the Herschel-constrained fits,  $\sim 6\%$  of our IR-bright sample qualifies as starbursts, slightly below the  $\sim 7\%$  inferred without Herschel and considerably lower than the  $< 20\%$  reported by Elbaz et al. (2011).

In contrast to Elbaz et al. (2011), we find that starburst galaxies do not elevate the median  $F_{\text{TIR}}/F_{7.7}$  ratio within any stellar mass bin. Instead, they com-

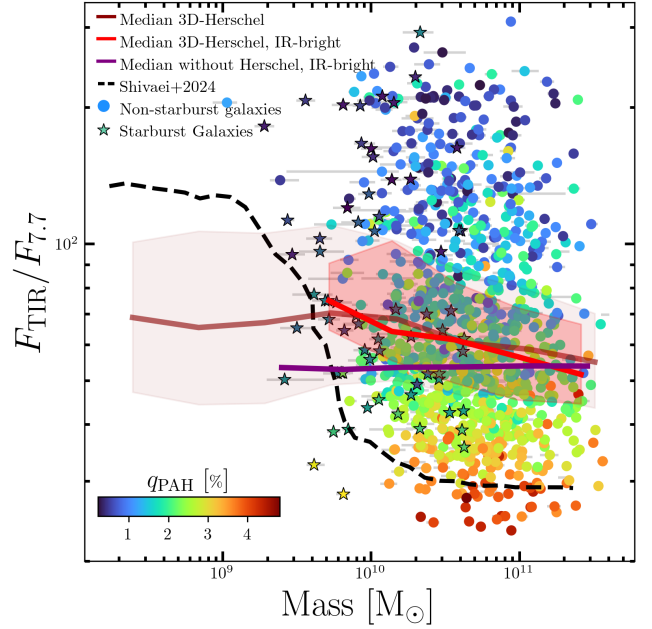


**Figure 9.** Estimates of  $F_{\text{TIR}}/F_{7.7}$  as a function of stellar mass for the IR-bright sample, using Herschel constraints. Scatter points are color-coded by the fraction of dust mass in PAHs, with starburst galaxies highlighted as stars. Median relations are shown for the full 3D-Herschel sample (red) and for the IR-bright sample inferred without FIR data with a fixed template (purple; equivalent to the  $24\mu\text{m}$ -to- $70\mu\text{m}$  color of the log-average of the Dale & Helou 2002 templates). The dashed line marks the mass- $F_{\text{TIR}}/F_{7.7}$  relation from Shivaie et al. (2024).

prise the majority of our FIR-bright objects below  $\log(M_*/M_\odot) \sim 10$ , reflecting both the limited depth of Herschel observations and the intrinsically FIR-bright nature of these systems. Including starburst galaxies is essential for extending the  $F_{\text{TIR}}/F_{7.7}$  relation to lower stellar masses and for identifying where UV-MIR fits underestimate the IR luminosity.

Our results show that the relative strength of MIR emission decreases with stellar mass, indicating that diffuse dust increasingly dominates the energy budget over PAH re-radiation in obscured, low-mass galaxies. The  $F_{\text{TIR}}/F_{7.7}$  ratio derived from 3D-Herschel fits displays substantial scatter, in contrast to the UV-MIR fits, which adopt fixed  $F_{\text{TIR}}$ -to- $F_{7.7}$  colors with a lower bound of  $\sim 53$  (median line, purple). At high stellar masses, the two methods converge, but in the lowest-mass bin ( $\log(M_*) \sim 9.6 M_\odot$ ), the UV-MIR fits underestimate  $F_{\text{TIR}}/F_{7.7}$  by  $\sim 0.2$  dex.

To illustrate the increase in  $F_{\text{TIR}}/F_{7.7}$  toward lower stellar masses, we present best-fit model composites of our IR-bright sample in bins of stellar mass in Figure 10. Each composite SED is normalized at  $1\mu\text{m}$  and calcu-

lated following the same procedure as in Figures 5 and 7. For clarity, the regions under the SEDs corresponding to  $F_{\text{TIR}}$  and  $F_{7.7}$  are shaded, and the legend indicates the fractional contribution of each mass bin to the full 3D-Herschel mass-limited sample within that range.

## 7. DISCUSSION

This study represents one of the first large-scale applications of `Prospector` to incorporate FIR constraints from Herschel into UV–MIR SED fits for a mass-complete galaxy sample at  $0.5 < z < 2.5$ . By directly anchoring the dust emission with FIR data, we test the reliability of MIR-based estimates of obscured star formation and explore how FIR information alters inferences of stellar populations and dust properties. The primary limitation of this approach lies in the quality of the FIR photometry. Herschel imaging is hampered by its broad PSF and relatively shallow depth, leading to poor resolution and significant source blending (see Section 2.2.1). To mitigate these effects, we applied a deblending procedure to extract forced photometric measurements, improving FIR flux estimates for faint sources (Lang et al. 2016). Nevertheless, a substantial fraction of our measurements remain upper limits (>90% in each Herschel band), particularly at the longest wavelengths. Despite these challenges, even upper limits provide meaningful constraints, as the addition of FIR photometry reduces uncertainties in key galaxy parameters.

### 7.1. Impact on the SFMS

Despite the challenges associated with Herschel data, we successfully incorporated FIR photometry (70–350 $\mu\text{m}$ ) into the 3D-HST catalogs and fit the resulting 3D-Herschel sample using `Prospector`. The FIR observations provide direct measurements of dust emission, yielding more precise estimates of attenuation and related galaxy properties. Overall, Herschel data demonstrate that UV–MIR priors can reasonably predict FIR fluxes and recover key parameters across a broad population (Figure 4). In our mass-limited sample of 34,443 galaxies,  $\sim 70$ –80% of objects have parameters consistent within  $1\sigma$  between the two sets of fits.

Importantly, we find that stellar masses inferred from UV–MIR data alone are robust for  $\sim 80\%$  of galaxies, while SFRs are reliable for  $\sim 70\%$ . As shown in Figure 8, the Herschel-constrained SFMS deviates by  $0.1 \pm 0.07$  dex on average relative to the UV–MIR inferred SFMS of Leja et al. (2022), with no observed systematic offset. The latter SFMS is derived using a similar Bayesian inference with `Prospector- $\alpha$`  modeling (and effectively the same UV–MIR data). Leja et al. (2022) measure

an SFMS with a normalization that is 0.2–0.5 dex lower than previous empirical estimates reported in the literature. Our results with FIR Herschel data generally corroborate these findings.

Although we find greater IR-to-MIR luminosity ratios at low to intermediate stellar masses when incorporating Herschel FIR photometry (see Figure 9), this increase in inferred SFRs appears mainly among the most highly obscured, IR-bright galaxies. For the majority of low-mass galaxies, the SFRs remain consistent with previous UV–MIR estimates (Figure 8). Constraining robust SFRs at low stellar masses remains challenging, however, as the PAH features diminish in strength (Shivaei et al. 2017). The sensitivity and technical capabilities of JWST, enabling SFR measurements for a wide range of methodologies, will further illuminate this particular regime. Given the prevalence of upper limits in our sample, this study would also benefit from deeper, higher-quality FIR observations. While we may not have another space-based FIR observatory in our lifetime, this study demonstrates that the MIR can serve as a robust proxy for estimating key stellar parameters.

### 7.2. Dust emission parameters

Incorporating FIR constraints enables a more informed analysis of the three dust emission parameters that shape the IR SED (Draine & Li 2007). In the absence of FIR data, it is common to fix these parameters or impose flat priors during modeling (Leja et al. 2019b, 2022; Shivaei et al. 2024), since MIR observations alone cannot fully constrain the total dust emission. The Draine & Li (2007) framework introduces  $q_{\text{PAH}}$ ,  $U_{\text{min}}$ , and  $\gamma$ :  $q_{\text{PAH}}$  is the fraction of dust mass in PAHs, which sets the strength of the MIR PAH features;  $U_{\text{min}}$  is the minimum starlight intensity heating the diffuse dust; and  $\gamma$  is the fraction of dust exposed to starlight intensities between  $U_{\text{min}} < U < U_{\text{max}}$ . Together,  $U_{\text{min}}$  and  $\gamma$  determine the shape and peak wavelength of the FIR dust bump, with higher  $U_{\text{min}}$  corresponding to warmer dust temperatures and shorter peak wavelengths, and values near  $U_{\text{min}} \sim 1$  indicate cooler dust temperatures (Casey et al. 2018). For a visualization of how these parameters influence the `Prospector`-modeled SED, see Leja et al. (2017).

In our UV–MIR fits, the dust emission parameters are fixed to  $U_{\text{min}} = 1$ ,  $q_{\text{PAH}} = 2$ , and  $\log(\gamma) = 2$ . Allowing them to vary in our 3D-Herschel fits shows that  $q_{\text{PAH}}$  and  $\log(\gamma)$  remain consistent with their fixed values, with standard deviations of 0.16 and 0.45 dex, respectively. By contrast,  $U_{\text{min}}$  is systematically larger, with a mean value of  $U_{\text{min}} = 7.1 \pm 3.1$  – about 0.85 dex higher than the fixed prior (right panel, Figure 11).

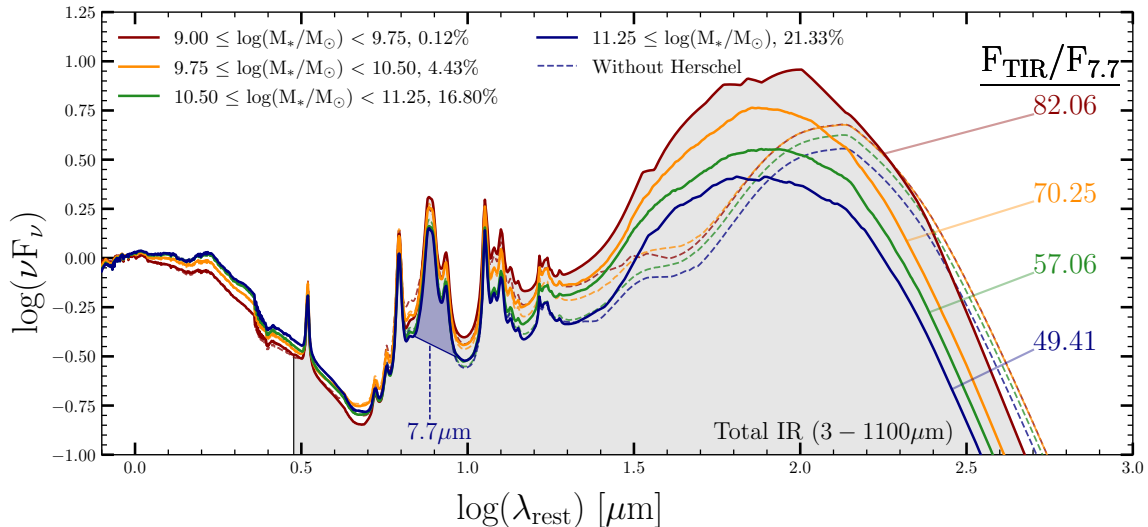


**Figure 10.** Composites from the IR-bright sample, binned by stellar mass, with the fractional contribution of each bin to the total sample for that mass range noted in the top left. Median  $F_{\text{TIR}}/F_{7.7}$  values of each composite are listed on the right, showing a decreasing trend with stellar mass. Shaded regions indicate the areas of integration for  $F_{\text{TIR}}$  and  $F_{7.7}$ .

Dust temperature can be estimated using the mean starlight intensity  $\langle U \rangle$ , following Equation (33) of [Draine & Li \(2007\)](#) – which is dependent on  $U_{\text{min}}$ ,  $U_{\text{max}}$ , and  $\gamma$  – and the characteristic dust temperature derived from Equation (13) of [Draine et al. \(2014\)](#):

$$T_{\text{d, char}} \approx 18 \langle U \rangle^{1/6} \text{ K.} \quad (4)$$

For the IR-bright sample, we calculate an average luminosity-weighted dust temperature of  $25.4 \pm 2.1\text{K}$  (black line in Figure 11), systematically warmer than the fixed cold dust temperature of 18.4K adopted in the UV–MIR fits (dashed navy line). The scatter (red line) in Figure 11 illustrates the distribution of  $U_{\text{min}}$  values, with a noticeable step to warmer temperatures at  $z \sim 1 - 1.3$ . This feature likely reflects a sampling bias, as Herschel preferentially detects higher-redshift star-forming galaxies with warm dust emission. Our results are consistent with [Muzzin et al. \(2010\)](#), who argued that high-redshift galaxies resemble “scaled-up cool galaxies” of their local counterparts, with relatively stable dust temperatures out to  $z \sim 2.5$ . However, they contrast with the findings of [Jones & Stanway \(2023\)](#), who report linearly increasing dust temperatures out to  $z \sim 10$ .

It is important to emphasize that we infer *characteristic* dust temperatures directly from our best-fit models, whereas other studies often adopt different definitions (e.g., effective dust temperature from the FIR peak wavelength ([Elbaz et al. 2011](#); [Casey et al. 2018](#); [Jones & Stanway 2023](#)). Any absolute comparison between these methods would therefore be misleading, and our results should be used only in a relative sense. Nevertheless, be-

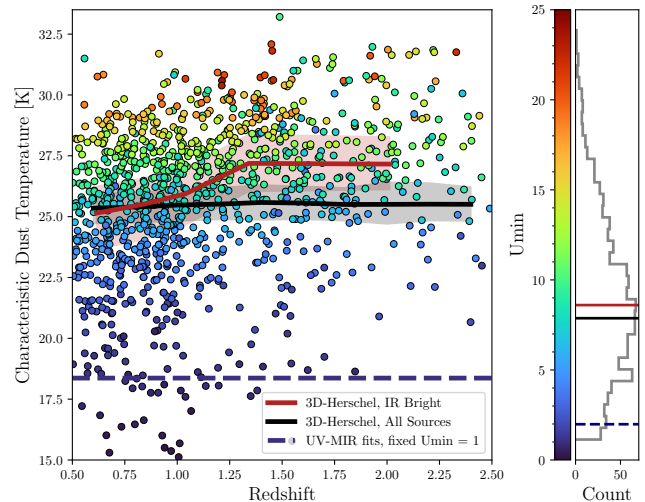


**Figure 11.** Characteristic dust temperature ( $T_{\text{d, char}}$ ; Equation 4) as a function of redshift for the IR-bright sample. Points are color-coded by  $U_{\text{min}}$ , with its distribution shown as a histogram along the color bar. Median reference lines mark the fixed  $U_{\text{min}}$  fits (dashed navy; 18.4K), the full 3D-Herschel mass-limited sample (black;  $25.4 \pm 2.1\text{K}$ ), and the IR-bright subsample (red;  $25.7 \pm 3.3\text{K}$ ).

cause the dust emission parameters we employ directly determine the FIR peak position, relative comparisons across studies remain meaningful. A more detailed examination, with a larger and more representative galaxy sample, will be required for a comprehensive reconciliation of dust temperature estimates in the literature.

The discrepancy between the estimated dust temperatures is further reflected in our empirical composite SEDs with Herschel constraints (Figures 5, 7, and

10). In the left panel of Figure 7, we compare galaxies whose SFRs and dust attenuation remain consistent with previous UV-MIR fits: both composites show similar FIR emission strengths, but the Herschel-informed spectrum has a broader FIR bump that peaks  $\sim 55\mu\text{m}$  shorter. In the right panel, galaxies with enhanced dust emission and SFRs exhibit even broader bumps with peaks shifted by  $\sim 62\mu\text{m}$  relative to UV-MIR fits. These shifts towards shorter peak wavelengths indicate: (1) a broader underlying dust temperature distribution, and (2) a systematically warmer characteristic dust temperature (see Casey 2012) compared to the model fits lacking FIR photometry.

Preliminary tests in Appendix C of Leja et al. (2017) measured dust emission parameters for 26 Herschel-imaged galaxies to motivate `Prospector` SED fitting without FIR data. In that study, tight priors reproduced Herschel observations most effectively, with an average  $U_{\text{min}} \sim 1$ . By contrast, our analysis finds that  $U_{\text{min}}$  is underestimated by a factor of  $\sim 7$  in such approaches, a discrepancy that may stem from the sample selection in Leja et al. (2017). First, the 26 galaxies were chosen to be “normal” L\* star-forming disks from the Kingfish survey (Kennicutt et al. 2011), and are all at  $z < 0.05$ , creating significant selection effects unrepresentative of our four-field wide study.

The characteristic dust temperature of a galaxy depends on multiple factors – including star formation activity, stellar population age, and the broader galaxy environment (e.g., the presence of AGNs Somerville & Davé 2015) – and underestimating the minimum starlight intensity risks skewing our understanding of dust composition and its role in galaxy evolution. Given the low resolution and shallow depth of Herschel imaging, this result requires validation with higher-resolution facilities such as ALMA or with next-generation FIR facilities such as PRIMA (Carpenter et al. 2020; Moullet et al. 2023).

### 7.3. IR-bright sample

We isolate a population of 1,118 IR-bright galaxies (Section 6), defined as sources with significant Spitzer/MIPS  $24\mu\text{m}$  detections ( $\text{SNR} > 3$ ) and detections in at least two Herschel bands. Compared to the full 3D-Herschel mass-limited samples, a larger fraction of these galaxies have best-fit parameters that fall outside the  $1\sigma$  limits ( $> 57\%$  for offsets driven by dust properties; Figure 6). Within the IR-bright sample, 73% of stellar mass estimates and 66% of SFR estimates remain consistent with the UV-MIR fits, slightly lower than the 78% and 70% agreement rates for the overall population of 34,443 galaxies.

As shown in Figure 6, the offsets are not unidirectional. Instead, a correlation between diffuse dust attenuation and SFR produces two comparably sized subpopulations: galaxies that are dustier, more star-forming, younger, somewhat less massive, and those that are less dusty, less star-forming, older, and more massive. Each subpopulation accounts for  $\sim 8\%$  of the IR-bright sample. These results highlight that a substantial fraction of highly obscured systems (up to 21% of our parent population; Table 6) are poorly captured by fixed MIR-to-FIR templates, which fail to reproduce the diversity of IR colors in these galaxies.

We find that greater dust attenuation correlates with higher SFRs, consistent with theoretical expectations: stars enrich the ISM with dust both during their formation and at the end of their lifetimes, making these processes concurrent in actively star-forming galaxies. By contrast, dust is destroyed on relatively short timescales (on the order of 100 Myr) in quiescent systems (Whitaker et al. 2021), though additional dust can be produced more than a gigayear later during the AGB phase (Conroy 2013; Höfner & Olofsson 2018).

Incorporating dust emission measurements helps break the well-known degeneracy between dust, age, and (to a lesser extent at high redshift) metallicity. Reducing this degeneracy minimizes uncertainties in stellar mass estimates that otherwise arise when only UV-MIR data are available (Conroy 2013; Leja et al. 2019b). Overall, our results demonstrate that `Prospector` UV-MIR fits provide a reliable tracer of the SFMS across a wide variety of galaxies, including most IR-bright objects when considering the average (Figure 8). At the lowest stellar masses within the IR-bright sample, however, there are hints of possible deviations.

We identify a small number of low-mass galaxies ( $\log(M_*/M_\odot) < 9.8$ ) at  $z \sim 1$  with underestimated  $\text{SFR}_{\text{IR}}$  by the UV-MIR fits. Whitaker et al. (2017) show that the fraction of obscured star formation ( $f_{\text{obscured}}$ ) generally increases with stellar mass, but also reveal a tail of highly obscured low-mass galaxies at  $z < 1$  and  $\log(M_*/M_\odot) \sim 9.4$ , where most galaxies exhibit  $f_{\text{obscured}} < 50\%$ . The obscured low-mass galaxies we identify contribute to this tail and have been largely overlooked in past studies, as their lack of PAH features (Shivaei et al. 2017) produce systematic underestimates of FIR emission using rigid, MIR-dependent templates. These extreme, low-mass starbursts comprise only a tiny fraction ( $\lesssim 0.1\%$ ) of the overall low-mass population, and MIR-to-IR conversions in the low-mass population as a whole remain model-dependent with large uncertainties (Elbaz et al. 2011; Whitaker et al. 2017; Shivaei et al. 2020, 2024).

The MIR range is dominated by PAH emission, with the strongest feature at  $7.7\mu\text{m}$ . In our comparison fits without FIR constraints, the MIPS  $24\mu\text{m}$  band is used as a proxy for the total IR luminosity. For galaxies at  $1.5 < z < 2.5$ , this corresponds to rest-frame  $\sim 8\mu\text{m}$  and is largely tracing the  $7.7\mu\text{m}$  PAH feature. The reliability of using PAH emission as a tracer of total IR output has been the subject of ongoing debate (Wuyts et al. 2008; Elbaz et al. 2011; Reddy et al. 2011; Shivaiei et al. 2017). Recent work has shown that the ratio  $F_{\text{TIR}}/F_{7.7}$  correlates with stellar mass (Shivaiei et al. 2024), likely reflecting the dependence of PAH abundance on stellar metallicity (Madden et al. 2006; Hunt et al. 2010; Seok et al. 2014; Xie & Ho 2019; Li 2020) together with the well-established mass-metallicity relation (Tremonti et al. 2004; Topping et al. 2021).

The formation and destruction of PAHs in the ISM is complex and involves multiple pathways. In the following subsection, we explore how these processes shape the observed offsets in  $F_{\text{TIR}}/F_{7.7}$  and place our results in the context of Shivaiei et al. (2024).

#### 7.4. MIR-to-IR luminosity relationship

In our analysis, the models constrained only by UV-MIR photometry convert Spitzer/MIPS  $24\mu\text{m}$  fluxes into total IR luminosity using the models from Draine & Li (2007) with parameters fixed such that  $L_8/L_{\text{IR}}$  follows the log-average of the Dale & Helou (2002) templates. At redshifts  $z \sim 1.5\text{--}2.5$ , the Spitzer/MIPS  $24\mu\text{m}$  bandpass captures the strong  $7.7\mu\text{m}$  PAH feature, which contributes  $\sim 40\text{--}50\%$  of the total PAH emission (Hunt et al. 2010) and serves as a widely used proxy for MIR output. However, studies have shown that relying on MIR emission to approximate  $L_{\text{IR}}$  and derive  $\text{SFR}_{\text{IR}}$  (e.g., Daddi et al. 2007; Wuyts et al. 2008; Whitaker et al. 2014), systematically underestimates both by a factor of  $\sim 2$  for galaxies with  $M_* \lesssim 10^{10} M_\odot$  and fails to recover  $L_{\text{IR}}$  accurately beyond  $z \sim 2$  (Elbaz et al. 2011; Schreiber et al. 2015; Shivaiei et al. 2017). By contrast, we find that including FIR photometry in our fits results in accurate  $\text{SFR}_{\text{IR}}$  and  $L_{\text{IR}}$  inferences for a majority of our parent sample.

As shown in Figure 9, the largest offsets in the  $F_{\text{TIR}}/F_{7.7}$  ratio – equivalent to  $L_{\text{IR}}/L_8$  – occur around  $\log(M_*/M_\odot) \sim 9.6$ , near the lower bound of our IR-bright sample. In this regime, Herschel-constrained fits yield  $F_{\text{TIR}}/F_{7.7}$  ratios larger by  $\sim 0.2$  dex compared to the UV-MIR fits, suggesting that Prospector models with fixed MIR-IR colors may systematically underpredict the total IR strength in low-mass systems.

The fixed MIR-IR colors in our models are governed by the three dust emission parameters— $\gamma$ ,  $U_{\text{min}}$ , and

most importantly,  $q_{\text{PAH}}$ , which represents the fraction of total dust mass in PAHs and is effectively equivalent to the ratio of MIR to total IR luminosity. When the dust parameters are fixed in the UV-MIR fits such that  $L_8/L_{\text{IR}}$  follows the log-average of the Dale & Helou (2002) templates, fits that additionally include Herschel FIR photometry yield free  $q_{\text{PAH}}$  estimates that exhibit a strong correlation with offsets in the inferred IR luminosity. Specifically, 14% of IR-bright sources show  $q_{\text{PAH}}$  values that are significantly overestimated when adopting a previously fixed value of  $q_{\text{PAH}} = 2$  (offsets exceeding the  $1\sigma$  uncertainty relative to the fixed- $q_{\text{PAH}}$  fits), corresponding to an average increase in the inferred IR luminosity of 0.27 dex and lower stellar mass estimates. Conversely, 10% of the IR-bright sample have  $q_{\text{PAH}}$  values that are significantly underestimated in the UV-MIR fits, leading to an average decrease in  $L_{\text{IR}}$  of 0.14 dex.

Previous work has found that the  $L_{\text{IR}}/L_8$  ratio remains nearly constant over most of cosmic history. Using the IRAC  $8\mu\text{m}$  bandpass, Elbaz et al. (2011) measured  $L_{\text{IR}}/L_8 = 4.9^{+2.9} - 2.2$  out to  $z \sim 2.5$ , while Reddy et al. (2011) reported  $7.7 \pm 1.6$  over a similar redshift range. A nearly constant  $L_{\text{IR}}/L_8$  ratio implies little evolution in the IR SED over this redshift range, a crucial factor when interpreting galaxy SEDs with limited IR coverage. Our results suggest, however, that low-mass IR-bright galaxies may deviate from this picture, highlighting the importance of direct FIR constraints in this regime.

The link between MIR emission and total IR output is not universal, as it depends critically on the abundance of PAHs. FIR templates are often used under the assumption that MIR emission scales proportionally with total IR emission across all galaxy types, but PAH production and survival are regulated by a galaxy’s physical and environmental conditions. PAHs are produced primarily in the ejecta of supernovae and in the carbon-rich outflows of AGB stars (Frenklach & Feigelson 1989; Galliano et al. 2008; Höfner & Olofsson 2018). Their formation is more efficient in high-metallicity environments, where shattering of carbonaceous dust grains replenishes the PAH population (Seok et al. 2014). On the other hand, low-metallicity systems exhibit reduced PAH production: either because young chemical environments lack sufficient gas-phase carbon to form PAHs (Draine et al. 2007), or because PAHs are destroyed by thermal sputtering in shock-heated, metal-poor gas with inefficient cooling (Li 2020). In addition, in environments without sufficient dust shielding, intense radiation fields can rapidly destroy PAHs (Madden et al. 2006; Hunt et al. 2010; Magdis et al. 2013; Shivaiei et al. 2017; Xie & Ho 2019).

In our modeling of the IR-bright sample, Nearly all sources exhibit elevated  $U_{\min}$  values, which also implies a suppression of  $F_{7.7}$  relative to  $F_{\text{TIR}}$ , consistent with expectations that PAHs are destroyed in stronger radiation fields (Madden et al. 2006; Hunt et al. 2010; Magdis et al. 2013; Shivaie et al. 2017; Xie & Ho 2019). We also find tentative evidence that some lower-metallicity galaxies exhibit increased SFRs (Figures 4 and 6). These systems show higher  $F_{\text{TIR-to-}F_{7.7}}$  ratios, consistent with the idea that metals provide dust shielding against intense UV radiation (Hunt et al. 2010; Magdis et al. 2013; Shivaie et al. 2017). Together, these trends suggest an interconnected picture: enhanced IR emission boosts the inferred SFRs, while stronger radiation fields in low-metallicity environments both heat the dust and suppress PAH survival. The observed rise in  $F_{\text{TIR}}/F_{7.7}$  therefore reflects the coupled influence of dust heating, metallicity, and PAH destruction.

### 7.5. Systematic Differences in $F_{\text{TIR}}/F_{7.7}$

In Figure 9, the  $F_{\text{TIR}}/F_{7.7}$  ratios estimated from fits with and without Herschel photometry agree at the massive end. However, the median trend from Shivaie et al. (2024) asymptotes to value that is lower by  $\sim 0.28$  dex relative to our measurements for galaxies  $\gtrsim 10^{10.3} M_{\odot}$ . Their analysis, based on JWST/MIRI data, compares the  $7.7\mu\text{m}$  PAH flux to the total IR flux ( $3\text{-}1100\mu\text{m}$ ) of star-forming galaxies using eight JWST/MIRI broadband filters spanning  $5.6\text{-}25.5\mu\text{m}$ . Our study, by contrast, relies on a single Spitzer/MIPS  $24\mu\text{m}$  measurement, which traces the rest-frame  $7.7\mu\text{m}$  feature only for galaxies at  $1.5 \lesssim z \lesssim 2.5$ . Shivaie et al. (2024) further find that the  $7.7\mu\text{m}$  PAH strength correlates strongly with stellar mass, following a logistic relation in which PAH emission increases towards higher masses, whereas we do not recover a strong stellar mass dependence in our work.

To investigate the origin of this discrepancy, we directly compare the inferred values from our work to that in Shivaie et al. (2024). Fortunately, the Systematic Mid-infrared Instrument Legacy Extragalactic Survey (SMILES; Rieke et al. 2024; Alberts et al. 2024) analyzed in Shivaie et al. (2024) lies within the GOODS-South field, which is also covered by 3D-Herschel, enabling a direct comparison between our inferred  $L_{\text{IR}}$  and  $L_{7.7}$  values and those reported by Shivaie et al. (2024). We quantify the scatter in both  $L_{\text{IR}}$  and  $L_{7.7}$  using the normalized median absolute deviation (NMAD). While the  $L_{\text{IR}}$  estimates show an NMAD of 0.18 dex with negligible median offset, the  $L_{7.7}$  values exhibit a larger scatter (NMAD = 0.27 dex) and are 0.27 dex systematically lower than those reported by Shivaie et al. (2024).

To test for calibration issues within our data, We examine the residuals between the observed MIPS  $24\mu\text{m}$  fluxes and the best-fit model prediction at the same wavelength. We find that the model fluxes are approximately 0.1 dex lower than the observed MIPS  $24\mu\text{m}$  fluxes, consistent with the lower  $L_{7.7}$  values we estimate relative to those in Shivaie et al. (2024). However, while this alleviates some tension, this does not fully account for the discrepancy. It is also worth noting that the Shivaie et al. (2024) analysis predates a significant update to the MIRI calibration, which resolved a systematic flux offset and may contribute to their higher inferred PAH luminosities.

Differences in the treatment of the dust-heating parameter  $U_{\min}$  may further contribute to the observed offset. In particular, Shivaie et al. (2024) adopt a flat prior for  $U_{\min}$  between 0.1-15 (Leja et al. 2017), whereas our modeling imposes a more conservative upper limit of 25. Roughly 9% of our IR-bright sample has  $U_{\min} > 15$ , corresponding to higher  $F_{\text{TIR}}/F_{7.7}$  values. While tighter priors on dust emission parameters can reduce biases and uncertainties in IR estimates without FIR data (Leja et al. 2017), as is the case for the Shivaie et al. (2024) analysis, allowing  $U_{\min}$  to exceed 15 provides flexibility to capture galaxies with more intense radiation field and elevated  $F_{\text{TIR}}/F_{7.7}$  ratios.

Taken together, the tension between this  $F_{\text{TIR}}/F_{7.7}$  ratios at intermediate-to-high stellar masses likely results from some combination of the following: (1) the  $U_{\min}$  prior adopted in Shivaie et al. (2024) may bias the average  $F_{\text{TIR}}/F_{7.7}$  ratios low, and (2) there may be residual systematics in the MIR flux calibrations in both studies. While we cannot definitively isolate the origin of this offset in  $F_{\text{TIR}}/F_{7.7}$ , this comparison highlights the importance of combining high-quality JWST data with wide-field, multi-survey analyses like ours to fully reconcile these measurements. Future facilities such as PRIMA will be critical for reopening a panoramic view of the MIR-to-FIR universe and for resolving remaining systematics in PAH-based IR diagnostics.

## 8. CONCLUSIONS

In this work, we incorporated FIR Herschel photometry ( $70 - 350\mu\text{m}$ ) into SED fitting of the 3D-HST photometric catalogs using the Bayesian modeling code `Prospector`. Because of the shallow depth and large PSF of the Herschel images, flux extraction requires sophisticated deblending techniques. Here, we perform ‘forced photometry’ with `MOPHONGO` and `T-PHOT`, enabling recovery of FIR fluxes down to fainter limits than otherwise possible. These measurements were added to the 3D-HST photometric catalog to produce a com-

prehensive, 0.3 - 350 $\mu$ m dataset, which we term 3D-Herschel and release publicly with this paper.

We validated the 3D-Herschel fluxes and source counts against independent Herschel analyses (§3). Flux comparisons (Figure 1) show consistency with published catalogs, while galaxy counts across the four fields and Herschel bands (Figure 2) confirm the reliability of the deblending pipeline.

With the validated 3D-Herschel catalogs, we performed SED fitting spanning the UV-FIR using `Prospector`. The addition of FIR data provided direct constraints on dust emission, allowing us to expand to a 17-parameter model that includes the three dust emission parameters –  $q_{\text{PAH}}$ ,  $\gamma$ , and  $U_{\text{min}}$  – which were previously fixed when modeling relied only on UV-MIR data.

The main findings of our analysis are summarized as follows:

1. The addition of Herschel FIR constraints to the fiducial UV-MIR fits does not significantly alter the majority of sources. Fitting UV-MIR photometry alone with `Prospector` reliably infers key galaxy properties and predicts  $L_{\text{IR}}$ , with  $\sim$ two-thirds of parameter offsets between UV-MIR and UV-FIR fits falling within the  $1\sigma$  uncertainties.
2. The inferred SFMS from UV-FIR photometry remains consistent with previous results based solely on UV-MIR constraints, validating the findings of Leja et al. (2022). The SFMS inferred herein shows no systematic offset from prior results, varying on average by  $0.1\pm 0.07$  dex and by no more than 0.25 dex in any given stellar mass bin.
3. Incorporating FIR photometry enables three additional free parameters –  $q_{\text{PAH}}$ ,  $\gamma$ , and  $U_{\text{min}}$  – to be constrained, whereas in the UV-MIR models they were fixed to correspond to cold dust temperatures, while our FIR-constrained field yield an average  $U_{\text{min}} = 7.1$ , implying dust temperatures  $\sim 7\text{K}$  warmer.
4. UV-MIR models rely on fixed IR templates that assume a constant  $F_{\text{TIR}}/F_{7.7}$  ratio across stellar mass. By contrast, fits to the IR-bright sample (spanning 0.1% of mass-limited sample at

$\log(M_*/M_\odot) = 9.5$  to  $\sim 20\%$  for  $\log(M_*/M_\odot) \geq 11.25$ ) show that  $F_{\text{TIR}}/F_{7.7}$  increases toward lower stellar masses, with a  $\sim 0.2$  dex offset from the UV-MIR fits at  $\log(M_*/M_\odot) \sim 9.6$ . This demonstrates that fixed IR templates underpredict FIR emission in the most obscured, low- to intermediate-mass galaxies.

The Herschel Space Observatory represents a past generation of space-based telescopes that opened a crucial window into the IR universe, albeit at limited resolution. In the upcoming era of advanced IR facilities, galaxy evolution studies will benefit from more sensitive, higher-resolution data, particularly in the MIR-FIR regime that remains largely inaccessible today. Our results, derived primarily from upper-limit constraints, highlight the substantial gains to be made in measuring key galaxy scaling relations with improved data. Looking ahead, future space missions with MIR-FIR coverage, together with FIR-to-submillimeter observations from facilities such as ALMA, will be essential to fully characterize the dust and star formation properties of galaxies.

- 1 Support for this work was provided by NASA through
- 2 the Astrophysics Data Analysis Program (ADAP) grant
- 3 80NSSC20K0416. Our research is made possible by the
- 4 use of the panchromatic SED modeling code `Prospector`.
- 5 Additionally, the use of the FSPS code in
- 6 `Prospector` has allowed us to compare robust mea-
- 7 surements of physical galaxy properties. We would like
- 8 to thank Stacey Alberts for their support in this study.
- 9 We acknowledge the EAZY SED modeling code as well
- 10 which our photometric redshifts have been taken from.
- 11 This research made use of `astrodendro`, a Python
- 12 package to compute dendrograms of Astronomical
- 13 data <http://www.dendrograms.org/>, as well as `Astropy`,
- 14 a community-developed core Python pack-
- 15 age for Astronomy (Astropy Collaboration, 2013),
- 16 <http://www.astropy.org>.
- 17 *Software:* `Prospector` (Johnson & Leja 2017), `python-`
- 18 `fsp`s (Foreman-Mackey et al. 2014), `Astropy` (Astropy
- 19 Collaboration et al. 2013, 2018), `FSPS` (Conroy et al.
- 20 2009), `matplotlib` (Caswell et al. 2020), `scipy` (Virtanen
- 21 et al. 2020), `ipython` (Perez & Granger 2007), `numpy`
- 22 (Van Der Walt et al. 2011).

## REFERENCES

- Abdurro’uf, Lin, Y.-T., Wu, P.-F., & Akiyama, M. 2021, *ApJS*, 254, 15, doi: 10.3847/1538-4365/abebe2
- Abramson, L. E., Gladders, M. D., Dressler, A., et al. 2015, *The Astrophysical Journal Letters*, 801, L12, doi: 10.1088/2041-8205/801/1/L12

- Acquaviva, V., Gawiser, E., & Guaita, L. 2011, *The Astrophysical Journal*, 737, 47, doi: [10.1088/0004-637X/737/2/47](https://doi.org/10.1088/0004-637X/737/2/47)
- Alberts, S., Lyu, J., Shivaeei, I., et al. 2024, SMILES Initial Data Release: Unveiling the Obscured Universe with MIRI Multi-band Imaging. <https://arxiv.org/abs/2405.15972>
- Ashby, M. L. N., Willner, S. P., Fazio, G. G., et al. 2013, *ApJ*, 769, 80, doi: [10.1088/0004-637X/769/1/80](https://doi.org/10.1088/0004-637X/769/1/80)
- Astropy Collaboration, Robitaille, T. P., Tollerud, E. J., et al. 2013, *A&A*, 558, A33, doi: [10.1051/0004-6361/201322068](https://doi.org/10.1051/0004-6361/201322068)
- Astropy Collaboration, Price-Whelan, A. M., Sipőcz, B. M., et al. 2018, *AJ*, 156, 123, doi: [10.3847/1538-3881/aabc4f](https://doi.org/10.3847/1538-3881/aabc4f)
- Behroozi, P. S., Wechsler, R. H., & Conroy, C. 2013, *ApJ*, 770, 57, doi: [10.1088/0004-637X/770/1/57](https://doi.org/10.1088/0004-637X/770/1/57)
- Bielby, R., Hudelot, P., McCracken, H. J., et al. 2012, *A&A*, 545, A23, doi: [10.1051/0004-6361/201118547](https://doi.org/10.1051/0004-6361/201118547)
- Boogaard, L. A., Brinchmann, J., Bouché, N., et al. 2018, *A&A*, 619, A27, doi: [10.1051/0004-6361/201833136](https://doi.org/10.1051/0004-6361/201833136)
- Boquien, M., Burgarella, D., Roehlly, Y., et al. 2019, *A&A*, 622, A103, doi: [10.1051/0004-6361/201834156](https://doi.org/10.1051/0004-6361/201834156)
- Bowman, W. P., Zeimann, G. R., Nagaraj, G., et al. 2020, *The Astrophysical Journal*, 899, 7, doi: [10.3847/1538-4357/ab9f3c](https://doi.org/10.3847/1538-4357/ab9f3c)
- Brammer, G. B., van Dokkum, P. G., & Coppi, P. 2008, *ApJ*, 686, 1503, doi: [10.1086/591786](https://doi.org/10.1086/591786)
- Brammer, G. B., Sánchez-Janssen, R., Labbé, I., et al. 2012, *ApJL*, 758, L17, doi: [10.1088/2041-8205/758/1/L17](https://doi.org/10.1088/2041-8205/758/1/L17)
- Brinchmann, J., & Ellis, R. S. 2000, *The Astrophysical Journal*, 536, L77, doi: [10.1086/312738](https://doi.org/10.1086/312738)
- Burgarella, D., Buat, V., & Iglesias-Páramo, J. 2005, *Monthly Notices of the Royal Astronomical Society*, 360, 1413, doi: [10.1111/j.1365-2966.2005.09131.x](https://doi.org/10.1111/j.1365-2966.2005.09131.x)
- Calzetti, D., Kennicutt, R. C., Engelbracht, C. W., et al. 2007, *ApJ*, 666, 870, doi: [10.1086/520082](https://doi.org/10.1086/520082)
- Capak, P., Cowie, L. L., Hu, E. M., et al. 2004, *AJ*, 127, 180, doi: [10.1086/380611](https://doi.org/10.1086/380611)
- Cardamone, C. N., van Dokkum, P. G., Urry, C. M., et al. 2010, *The Astrophysical Journal Supplement Series*, 189, 270, doi: [10.1088/0067-0049/189/2/270](https://doi.org/10.1088/0067-0049/189/2/270)
- Carnall, A. C., Leja, J., Johnson, B. D., et al. 2019, *The Astrophysical Journal*, 873, 44, doi: [10.3847/1538-4357/ab04a2](https://doi.org/10.3847/1538-4357/ab04a2)
- Carnall, A. C., McLure, R. J., Dunlop, J. S., & Davé, R. 2018, *Monthly Notices of the Royal Astronomical Society*, 480, 4379, doi: [10.1093/mnras/sty2169](https://doi.org/10.1093/mnras/sty2169)
- Carpenter, J., Iono, D., Kemper, F., & Wootten, A. 2020, *arXiv e-prints*, arXiv:2001.11076, doi: [10.48550/arXiv.2001.11076](https://doi.org/10.48550/arXiv.2001.11076)
- Casey, C. M. 2012, *MNRAS*, 425, 3094, doi: [10.1111/j.1365-2966.2012.21455.x](https://doi.org/10.1111/j.1365-2966.2012.21455.x)
- Casey, C. M., Hodge, J., Zavala, J. A., et al. 2018, *ApJ*, 862, 78, doi: [10.3847/1538-4357/aacd11](https://doi.org/10.3847/1538-4357/aacd11)
- Caswell, T. A., Droettboom, M., Lee, A., et al. 2020, *matplotlib/matplotlib: REL: v3.2.1, v3.2.1*, Zenodo, doi: [10.5281/zenodo.3714460](https://doi.org/10.5281/zenodo.3714460)
- Chabrier, G. 2003, *PASP*, 115, 763, doi: [10.1086/376392](https://doi.org/10.1086/376392)
- Charlot, S., & Fall, S. M. 2000, *ApJ*, 539, 718, doi: [10.1086/309250](https://doi.org/10.1086/309250)
- Conroy, C. 2013, *ARA&A*, 51, 393, doi: [10.1146/annurev-astro-082812-141017](https://doi.org/10.1146/annurev-astro-082812-141017)
- Conroy, C., Gunn, J. E., & White, M. 2009, *ApJ*, 699, 486, doi: [10.1088/0004-637X/699/1/486](https://doi.org/10.1088/0004-637X/699/1/486)
- Da Cunha, E., Charlot, S., & Elbaz, D. 2008, *Monthly Notices of the Royal Astronomical Society*, 388, 1595, doi: [10.1111/j.1365-2966.2008.13535.x](https://doi.org/10.1111/j.1365-2966.2008.13535.x)
- Daddi, E., Dickinson, M., Morrison, G., et al. 2007, *The Astrophysical Journal*, 670, 156, doi: [10.1086/521818](https://doi.org/10.1086/521818)
- Dale, D. A., & Helou, G. 2002, *ApJ*, 576, 159, doi: [10.1086/341632](https://doi.org/10.1086/341632)
- Davé, R., Anglés-Alcázar, D., Narayanan, D., et al. 2019, *MNRAS*, 486, 2827, doi: [10.1093/mnras/stz937](https://doi.org/10.1093/mnras/stz937)
- Dickinson, M., Giavalisco, M., & team, t. G. 2003, in *The Mass of Galaxies at Low and High Redshift: Proceedings of the European Southern Observatory and Universitäts-Sternwarte München Workshop Held in Venice, Italy, 24-26 October 2001*, Springer, 324–331
- Draine, B. T., & Li, A. 2007, *The Astrophysical Journal*, 657, 810, doi: [10.1086/511055](https://doi.org/10.1086/511055)
- Draine, B. T., Li, A., Hensley, B. S., et al. 2021, *ApJ*, 917, 3, doi: [10.3847/1538-4357/abff51](https://doi.org/10.3847/1538-4357/abff51)
- Draine, B. T., Dale, D. A., Bendo, G., et al. 2007, *ApJ*, 663, 866, doi: [10.1086/518306](https://doi.org/10.1086/518306)
- Draine, B. T., Aniano, G., Krause, O., et al. 2014, *ApJ*, 780, 172, doi: [10.1088/0004-637X/780/2/172](https://doi.org/10.1088/0004-637X/780/2/172)
- Elbaz, D., Daddi, E., Le Borgne, D., et al. 2007, *A&A*, 468, 33, doi: [10.1051/0004-6361:20077525](https://doi.org/10.1051/0004-6361:20077525)
- Elbaz, D., Dickinson, M., Hwang, H. S., et al. 2011, *A&A*, 533, A119, doi: [10.1051/0004-6361/201117239](https://doi.org/10.1051/0004-6361/201117239)
- Erben, T., Schirmer, M., Dietrich, J. P., et al. 2005, *Astronomische Nachrichten*, 326, 432, doi: [10.1002/asna.200510396](https://doi.org/10.1002/asna.200510396)
- Erben, T., Hildebrandt, H., Lerchster, M., et al. 2009, *A&A*, 493, 1197, doi: [10.1051/0004-6361:200810426](https://doi.org/10.1051/0004-6361:200810426)
- Foreman-Mackey, D., Sick, J., & Johnson, B. 2014, *python-fsps: Python bindings to FSPPS (v0.1.1)*, v0.1.1, Zenodo, doi: [10.5281/zenodo.12157](https://doi.org/10.5281/zenodo.12157)
- Frenklach, M., & Feigelson, E. D. 1989, *ApJ*, 341, 372, doi: [10.1086/167501](https://doi.org/10.1086/167501)

- Fumagalli, M., Labbé, I., Patel, S. G., et al. 2014, *ApJ*, 796, 35, doi: [10.1088/0004-637X/796/1/35](https://doi.org/10.1088/0004-637X/796/1/35)
- Furlong, M., Bower, R. G., Theuns, T., et al. 2015, *MNRAS*, 450, 4486, doi: [10.1093/mnras/stv852](https://doi.org/10.1093/mnras/stv852)
- Furusawa, H., Kosugi, G., Akiyama, M., et al. 2008, *ApJS*, 176, 1, doi: [10.1086/527321](https://doi.org/10.1086/527321)
- Galliano, F., Dwek, E., & Charnial, P. 2008, *ApJ*, 672, 214, doi: [10.1086/523621](https://doi.org/10.1086/523621)
- Gardner, J. P., Mather, J. C., Abbott, R., et al. 2023, *PASP*, 135, 068001, doi: [10.1088/1538-3873/acd1b5](https://doi.org/10.1088/1538-3873/acd1b5)
- Giavalisco, M., Ferguson, H. C., Koekemoer, A. M., et al. 2004, *ApJL*, 600, L93, doi: [10.1086/379232](https://doi.org/10.1086/379232)
- Grogin, N. A., Kocevski, D. D., Faber, S. M., et al. 2011, *ApJS*, 197, 35, doi: [10.1088/0067-0049/197/2/35](https://doi.org/10.1088/0067-0049/197/2/35)
- Han, Y., & Han, Z. 2014, *The Astrophysical Journal Supplement Series*, 215, 2, doi: [10.1088/0067-0049/215/1/2](https://doi.org/10.1088/0067-0049/215/1/2)
- Hayward, C. C., & Smith, D. J. B. 2015, *MNRAS*, 446, 1512, doi: [10.1093/mnras/stu2195](https://doi.org/10.1093/mnras/stu2195)
- Hildebrandt, H., Pielorz, J., Erben, T., et al. 2009, *A&A*, 498, 725, doi: [10.1051/0004-6361/200811042](https://doi.org/10.1051/0004-6361/200811042)
- Hildebrandt, H., Erben, T., Dietrich, J. P., et al. 2006, *A&A*, 452, 1121, doi: [10.1051/0004-6361:20054278](https://doi.org/10.1051/0004-6361:20054278)
- Höfner, S., & Olofsson, H. 2018, *A&A Rv*, 26, 1, doi: [10.1007/s00159-017-0106-5](https://doi.org/10.1007/s00159-017-0106-5)
- Hsieh, B.-C., Wang, W.-H., Hsieh, C.-C., et al. 2012, *The Astrophysical Journal Supplement Series*, 203, 23, doi: [10.1088/0067-0049/203/2/23](https://doi.org/10.1088/0067-0049/203/2/23)
- Hunt, L. K., Thuan, T. X., Izotov, Y. I., & Sauvage, M. 2010, *ApJ*, 712, 164, doi: [10.1088/0004-637X/712/1/164](https://doi.org/10.1088/0004-637X/712/1/164)
- Iyer, K. G., Gawiser, E., Faber, S. M., et al. 2019, *ApJ*, 879, 116, doi: [10.3847/1538-4357/ab2052](https://doi.org/10.3847/1538-4357/ab2052)
- Jin, S., Daddi, E., Liu, D., et al. 2018, *ApJ*, 864, 56, doi: [10.3847/1538-4357/aad4af](https://doi.org/10.3847/1538-4357/aad4af)
- Johnson, B., & Leja, J. 2017, *Bd-J/Prospector: Initial Release, v0.1*, Zenodo, Zenodo, doi: [10.5281/zenodo.1116491](https://doi.org/10.5281/zenodo.1116491)
- Johnson, B. D., Leja, J., Conroy, C., & Speagle, J. S. 2021, *ApJS*, 254, 22, doi: [10.3847/1538-4365/abef67](https://doi.org/10.3847/1538-4365/abef67)
- Jones, G. T., & Stanway, E. R. 2023, *MNRAS*, 525, 5720, doi: [10.1093/mnras/stad2683](https://doi.org/10.1093/mnras/stad2683)
- Kajisawa, M., Ichikawa, T., Tanaka, I., et al. 2011, *Publications of the Astronomical Society of Japan*, 63, S379, doi: [10.1093/pasj/63.sp2.S379](https://doi.org/10.1093/pasj/63.sp2.S379)
- Kennicutt, Robert C., J., Hao, C.-N., Calzetti, D., et al. 2009, *ApJ*, 703, 1672, doi: [10.1088/0004-637X/703/2/1672](https://doi.org/10.1088/0004-637X/703/2/1672)
- Kennicutt, R. C., & Evans, N. J. 2012, *Annual Review of Astronomy and Astrophysics*, 50, 531, doi: [10.1146/annurev-astro-081811-125610](https://doi.org/10.1146/annurev-astro-081811-125610)
- Kennicutt, R. C., Calzetti, D., Aniano, G., et al. 2011, *Publications of the Astronomical Society of the Pacific*, 123, 1347, doi: [10.1086/663818](https://doi.org/10.1086/663818)
- Kirkpatrick, A., Pope, A., Alexander, D. M., et al. 2012, *ApJ*, 759, 139, doi: [10.1088/0004-637X/759/2/139](https://doi.org/10.1088/0004-637X/759/2/139)
- Koekemoer, A. M., Faber, S. M., Ferguson, H. C., et al. 2011, *ApJS*, 197, 36, doi: [10.1088/0067-0049/197/2/36](https://doi.org/10.1088/0067-0049/197/2/36)
- Kriek, M., & Conroy, C. 2013, *ApJL*, 775, L16, doi: [10.1088/2041-8205/775/1/L16](https://doi.org/10.1088/2041-8205/775/1/L16)
- Kriek, M., van Dokkum, P. G., Labbé, I., et al. 2009, *ApJ*, 700, 221, doi: [10.1088/0004-637X/700/1/221](https://doi.org/10.1088/0004-637X/700/1/221)
- Kurczynski, P., Gawiser, E., Acquaviva, V., et al. 2016, *ApJL*, 820, L1, doi: [10.3847/2041-8205/820/1/L1](https://doi.org/10.3847/2041-8205/820/1/L1)
- Labbé, I., Bouwens, R., Illingworth, G. D., & Franx, M. 2006, *ApJL*, 649, L67, doi: [10.1086/508512](https://doi.org/10.1086/508512)
- Lang, D., Hogg, D. W., & Schlegel, D. J. 2016, *AJ*, 151, 36, doi: [10.3847/0004-6256/151/2/36](https://doi.org/10.3847/0004-6256/151/2/36)
- Lee, N., Sanders, D. B., Casey, C. M., et al. 2015, *ApJ*, 801, 80, doi: [10.1088/0004-637X/801/2/80](https://doi.org/10.1088/0004-637X/801/2/80)
- Leja, J., Carnall, A. C., Johnson, B. D., Conroy, C., & Speagle, J. S. 2019a, *ApJ*, 876, 3, doi: [10.3847/1538-4357/ab133c](https://doi.org/10.3847/1538-4357/ab133c)
- Leja, J., Johnson, B. D., Conroy, C., van Dokkum, P. G., & Byler, N. 2017, *ApJ*, 837, 170, doi: [10.3847/1538-4357/aa5ffe](https://doi.org/10.3847/1538-4357/aa5ffe)
- Leja, J., Johnson, B. D., Conroy, C., et al. 2019b, *ApJ*, 877, 140, doi: [10.3847/1538-4357/ab1d5a](https://doi.org/10.3847/1538-4357/ab1d5a)
- Leja, J., Speagle, J. S., Ting, Y.-S., et al. 2022, *ApJ*, 936, 165, doi: [10.3847/1538-4357/ac887d](https://doi.org/10.3847/1538-4357/ac887d)
- Li, A. 2020, *Nature Astronomy*, 4, 339, doi: [10.1038/s41550-020-1051-1](https://doi.org/10.1038/s41550-020-1051-1)
- Liu, D., Daddi, E., Dickinson, M., et al. 2018, *ApJ*, 853, 172, doi: [10.3847/1538-4357/aaa600](https://doi.org/10.3847/1538-4357/aaa600)
- Lutz, D., Poglitsch, A., Altieri, B., et al. 2011, *A&A*, 532, A90, doi: [10.1051/0004-6361/201117107](https://doi.org/10.1051/0004-6361/201117107)
- Madau, P., & Dickinson, M. 2014, *ARA&A*, 52, 415, doi: [10.1146/annurev-astro-081811-125615](https://doi.org/10.1146/annurev-astro-081811-125615)
- Madden, S. C., Galliano, F., Jones, A. P., & Sauvage, M. 2006, *A&A*, 446, 877, doi: [10.1051/0004-6361:20053890](https://doi.org/10.1051/0004-6361:20053890)
- Magdis, G. E., Rigopoulou, D., Helou, G., et al. 2013, *A&A*, 558, A136, doi: [10.1051/0004-6361/201322226](https://doi.org/10.1051/0004-6361/201322226)
- Magnelli, B., Popesso, P., Berta, S., et al. 2013, *A&A*, 553, A132, doi: [10.1051/0004-6361/201321371](https://doi.org/10.1051/0004-6361/201321371)
- Maraston, C., Pforr, J., Renzini, A., et al. 2010, *Monthly Notices of the Royal Astronomical Society*, 407, 830, doi: [10.1111/j.1365-2966.2010.16973.x](https://doi.org/10.1111/j.1365-2966.2010.16973.x)
- Mathews, E. P., Leja, J., Speagle, J. S., et al. 2023, *The Astrophysical Journal*, 954, 132, doi: [10.3847/1538-4357/ace720](https://doi.org/10.3847/1538-4357/ace720)

- McCracken, H. J., Milvang-Jensen, B., Dunlop, J., et al. 2012, *A&A*, 544, A156, doi: [10.1051/0004-6361/201219507](https://doi.org/10.1051/0004-6361/201219507)
- Merlin, E., Fontana, A., Ferguson, H. C., et al. 2015, *A&A*, 582, A15, doi: [10.1051/0004-6361/201526471](https://doi.org/10.1051/0004-6361/201526471)
- Merlin, E., Bourne, N., Castellano, M., et al. 2016, *A&A*, 595, A97, doi: [10.1051/0004-6361/201628751](https://doi.org/10.1051/0004-6361/201628751)
- Momcheva, I. G., Brammer, G. B., van Dokkum, P. G., et al. 2016, *ApJS*, 225, 27, doi: [10.3847/0067-0049/225/2/27](https://doi.org/10.3847/0067-0049/225/2/27)
- Mouillet, A., Kataria, T., Lis, D., et al. 2023, arXiv e-prints, arXiv:2310.20572, doi: [10.48550/arXiv.2310.20572](https://doi.org/10.48550/arXiv.2310.20572)
- Muzzin, A., van Dokkum, P., Kriek, M., et al. 2010, *ApJ*, 725, 742, doi: [10.1088/0004-637X/725/1/742](https://doi.org/10.1088/0004-637X/725/1/742)
- Nelson, E. J., Tacchella, S., Diemer, B., et al. 2021, *MNRAS*, 508, 219, doi: [10.1093/mnras/stab2131](https://doi.org/10.1093/mnras/stab2131)
- Nguyen, H. T., Schulz, B., Levenson, L., et al. 2010, *A&A*, 518, L5, doi: [10.1051/0004-6361/201014680](https://doi.org/10.1051/0004-6361/201014680)
- Noeske, K. G., Weiner, B. J., Faber, S. M., et al. 2007, *ApJL*, 660, L43, doi: [10.1086/517926](https://doi.org/10.1086/517926)
- Noll, S., Burgarella, D., Giovannoli, E., et al. 2009, *A&A*, 507, 1793, doi: [10.1051/0004-6361/200912497](https://doi.org/10.1051/0004-6361/200912497)
- Nonino, M., Dickinson, M., Rosati, P., et al. 2009, *ApJS*, 183, 244, doi: [10.1088/0067-0049/183/2/244](https://doi.org/10.1088/0067-0049/183/2/244)
- Oliver, S. J., Bock, J., Altieri, B., et al. 2012, *MNRAS*, 424, 1614, doi: [10.1111/j.1365-2966.2012.20912.x](https://doi.org/10.1111/j.1365-2966.2012.20912.x)
- Pacifici, C., Iyer, K. G., Mobasher, B., et al. 2023, *ApJ*, 944, 141, doi: [10.3847/1538-4357/acacff](https://doi.org/10.3847/1538-4357/acacff)
- Papovich, C., Dickinson, M., & Ferguson, H. C. 2001, *ApJ*, 559, 620, doi: [10.1086/322412](https://doi.org/10.1086/322412)
- Perez, F., & Granger, B. E. 2007, *Computing in Science and Engineering*, 9, 21, doi: [10.1109/MCSE.2007.53](https://doi.org/10.1109/MCSE.2007.53)
- Pope, A., Scott, D., Dickinson, M., et al. 2008, in *Astronomical Society of the Pacific Conference Series*, Vol. 381, *Infrared Diagnostics of Galaxy Evolution*, ed. R. R. Chary, H. I. Teplitz, & K. Sheth, 249
- Popesso, P., Magnelli, B., Buttiglione, S., et al. 2012, arXiv e-prints, arXiv:1211.4257, doi: [10.48550/arXiv.1211.4257](https://doi.org/10.48550/arXiv.1211.4257)
- Popesso, P., Morselli, L., Concas, A., et al. 2019, *Monthly Notices of the Royal Astronomical Society*, 490, 5285, doi: [10.1093/mnras/stz2635](https://doi.org/10.1093/mnras/stz2635)
- Reddy, N., Dickinson, M., Elbaz, D., et al. 2011, *The Astrophysical Journal*, 744, 154, doi: [10.1088/0004-637X/744/2/154](https://doi.org/10.1088/0004-637X/744/2/154)
- Renzini, A., & Peng, Y.-j. 2015, *ApJL*, 801, L29, doi: [10.1088/2041-8205/801/2/L29](https://doi.org/10.1088/2041-8205/801/2/L29)
- Retzlaff, J., Rosati, P., Dickinson, M., et al. 2010, *A&A*, 511, A50, doi: [10.1051/0004-6361/200912940](https://doi.org/10.1051/0004-6361/200912940)
- Rieke, G. H., Alberts, S., Shivaiei, I., et al. 2024, *ApJ*, 975, 83, doi: [10.3847/1538-4357/ad6cd2](https://doi.org/10.3847/1538-4357/ad6cd2)
- Rieke, G. H., Young, E. T., Engelbracht, C. W., et al. 2004, *ApJS*, 154, 25, doi: [10.1086/422717](https://doi.org/10.1086/422717)
- Rieke, G. H., Wright, G. S., Böker, T., et al. 2015, *PASP*, 127, 584, doi: [10.1086/682252](https://doi.org/10.1086/682252)
- Roseboom, I. G., Oliver, S. J., Kunz, M., et al. 2010, *MNRAS*, 409, 48, doi: [10.1111/j.1365-2966.2010.17634.x](https://doi.org/10.1111/j.1365-2966.2010.17634.x)
- Rujopakarn, W., Rieke, G. H., Weiner, B. J., et al. 2013, *ApJ*, 767, 73, doi: [10.1088/0004-637X/767/1/73](https://doi.org/10.1088/0004-637X/767/1/73)
- Salim, S., Rich, R. M., Charlot, S., et al. 2007, *The Astrophysical Journal Supplement Series*, 173, 267, doi: [10.1086/519218](https://doi.org/10.1086/519218)
- Sanders, D. B., & Mirabel, I. F. 1996, *ARA&A*, 34, 749, doi: [10.1146/annurev.astro.34.1.749](https://doi.org/10.1146/annurev.astro.34.1.749)
- Sanders, D. B., Salvato, M., Aussel, H., et al. 2007, *ApJS*, 172, 86, doi: [10.1086/517885](https://doi.org/10.1086/517885)
- Schreiber, C., Pannella, M., Elbaz, D., et al. 2015, *A&A*, 575, A74, doi: [10.1051/0004-6361/201425017](https://doi.org/10.1051/0004-6361/201425017)
- Schreiber, C., Glazebrook, K., Nanayakkara, T., et al. 2018, *A&A*, 618, A85, doi: [10.1051/0004-6361/201833070](https://doi.org/10.1051/0004-6361/201833070)
- Seok, J. Y., Hirashita, H., & Asano, R. S. 2014, *MNRAS*, 439, 2186, doi: [10.1093/mnras/stu120](https://doi.org/10.1093/mnras/stu120)
- Shapley, A. E., Steidel, C. C., Adelberger, K. L., et al. 2001, *The Astrophysical Journal*, 562, 95, doi: [10.1086/323432](https://doi.org/10.1086/323432)
- Shivaiei, I., Darvish, B., Sattari, Z., et al. 2020, *ApJL*, 903, L28, doi: [10.3847/2041-8213/abc1ef](https://doi.org/10.3847/2041-8213/abc1ef)
- Shivaiei, I., Reddy, N. A., Shapley, A. E., et al. 2017, *ApJ*, 837, 157, doi: [10.3847/1538-4357/aa619c](https://doi.org/10.3847/1538-4357/aa619c)
- Shivaiei, I., Alberts, S., Florian, M., et al. 2024, *A&A*, 690, A89, doi: [10.1051/0004-6361/202449579](https://doi.org/10.1051/0004-6361/202449579)
- Skelton, R. E., Whitaker, K. E., Momcheva, I. G., et al. 2014, *ApJS*, 214, 24, doi: [10.1088/0067-0049/214/2/24](https://doi.org/10.1088/0067-0049/214/2/24)
- Somerville, R. S., & Davé, R. 2015, *Annual Review of Astronomy and Astrophysics*, 53, 51, doi: [10.1146/annurev-astro-082812-140951](https://doi.org/10.1146/annurev-astro-082812-140951)
- Speagle, J. S., Steinhardt, C. L., Capak, P. L., & Silverman, J. D. 2014, *The Astrophysical Journal Supplement Series*, 214, 15, doi: [10.1088/0067-0049/214/2/15](https://doi.org/10.1088/0067-0049/214/2/15)
- Steidel, C. C., Adelberger, K. L., Shapley, A. E., et al. 2003, *ApJ*, 592, 728, doi: [10.1086/375772](https://doi.org/10.1086/375772)
- Tal, T., Dekel, A., Oesch, P., et al. 2014, *ApJ*, 789, 164, doi: [10.1088/0004-637X/789/2/164](https://doi.org/10.1088/0004-637X/789/2/164)
- Taniguchi, Y., Scoville, N., Murayama, T., et al. 2007, *The Astrophysical Journal Supplement Series*, 172, 9, doi: [10.1086/516596](https://doi.org/10.1086/516596)
- Tomczak, A. R., Quadri, R. F., Tran, K.-V. H., et al. 2016, *ApJ*, 817, 118, doi: [10.3847/0004-637X/817/2/118](https://doi.org/10.3847/0004-637X/817/2/118)
- Topping, M. W., Shapley, A. E., Sanders, R. L., et al. 2021, *MNRAS*, 506, 1237, doi: [10.1093/mnras/stab1793](https://doi.org/10.1093/mnras/stab1793)

- Tremonti, C. A., Heckman, T. M., Kauffmann, G., et al. 2004, *The Astrophysical Journal*, 613, 898, doi: [10.1086/423264](https://doi.org/10.1086/423264)
- Utomo, D., Kriek, M., Labbé, I., Conroy, C., & Fumagalli, M. 2014, *ApJL*, 783, L30, doi: [10.1088/2041-8205/783/2/L30](https://doi.org/10.1088/2041-8205/783/2/L30)
- Van Der Walt, S., Colbert, S. C., & Varoquaux, G. 2011, *Computing in Science and Engineering*, 13, 22, doi: [10.1109/MCSE.2011.37](https://doi.org/10.1109/MCSE.2011.37)
- van Dokkum, P. G., Nelson, E. J., Franx, M., et al. 2015, *ApJ*, 813, 23, doi: [10.1088/0004-637X/813/1/23](https://doi.org/10.1088/0004-637X/813/1/23)
- Virtanen, P., Gommers, R., Oliphant, T. E., et al. 2020, *Nature Medicine*, 17, 261, doi: [10.1038/s41592-019-0686-2](https://doi.org/10.1038/s41592-019-0686-2)
- Wang, B., Leja, J., Bezanson, R., et al. 2023, *The Astrophysical Journal Letters*, 944, L58, doi: [10.3847/2041-8213/acba99](https://doi.org/10.3847/2041-8213/acba99)
- Whitaker, K. E., Pope, A., Cybulski, R., et al. 2017, *The Astrophysical Journal*, 850, 208, doi: [10.3847/1538-4357/aa94ce](https://doi.org/10.3847/1538-4357/aa94ce)
- Whitaker, K. E., van Dokkum, P. G., Brammer, G., & Franx, M. 2012, *ApJL*, 754, L29, doi: [10.1088/2041-8205/754/2/L29](https://doi.org/10.1088/2041-8205/754/2/L29)
- Whitaker, K. E., Labbé, I., van Dokkum, P. G., et al. 2011, *ApJ*, 735, 86, doi: [10.1088/0004-637X/735/2/86](https://doi.org/10.1088/0004-637X/735/2/86)
- Whitaker, K. E., Franx, M., Leja, J., et al. 2014, *ApJ*, 795, 104, doi: [10.1088/0004-637X/795/2/104](https://doi.org/10.1088/0004-637X/795/2/104)
- Whitaker, K. E., Narayanan, D., Williams, C. C., et al. 2021, *The Astrophysical Journal Letters*, 922, L30, doi: [10.3847/2041-8213/ac399f](https://doi.org/10.3847/2041-8213/ac399f)
- Wright, G. S., Rieke, G. H., Glasse, A., et al. 2023, *PASP*, 135, 048003, doi: [10.1088/1538-3873/acbe66](https://doi.org/10.1088/1538-3873/acbe66)
- Wuyts, S., Labbé, I., Förster Schreiber, N. M., et al. 2008, *ApJ*, 682, 985, doi: [10.1086/588749](https://doi.org/10.1086/588749)
- Xie, Y., & Ho, L. C. 2019, *ApJ*, 884, 136, doi: [10.3847/1538-4357/ab4200](https://doi.org/10.3847/1538-4357/ab4200)